Monthly Modulations of ENSO Teleconnections: Implications for Potential Predictability in North America

WILLIAM E. CHAPMAN,[a] ANEESH C. SUBRAMANIAN,[b] SHANG-PING XIE,[a] MICHAEL D. SIERKS,[a] F. MARTIN RALPH,[a] AND YOUICHI KAMAE[c]

[a] *Scripps Institution of Oceanography, University of California San Diego, La Jolla, California*
[b] *University of Colorado Boulder, Boulder, Colorado*
[c] *Faculty of Life and Environmental Sciences, University of Tsukuba, Tsukuba, Ibaraki, Japan*

(Manuscript received 25 May 2020, in final form 1 January 2021)

ABSTRACT: Using a high-resolution atmospheric general circulation model simulation of unprecedented ensemble size, we examine potential predictability of monthly anomalies under El Niño–Southern Oscillation (ENSO) forcing and background internal variability. This study reveals the pronounced month-to-month evolution of both the ENSO forcing signal and internal variability. Internal variance in upper-level geopotential height decreases (~10%) over the North Pacific during El Niño as the westerly jet extends eastward, allowing forced signals to account for a greater fraction of the total variability, and leading to increased potential predictability. We identify February and March of El Niño years as the most predictable months using a signal-to-noise analysis. In contrast, December, a month typically included in teleconnection studies, shows little to no potential predictability. We show that the seasonal evolution of SST forcing and variability leads to significant signal-to-noise relationships that can be directly linked to both upper-level and surface variable predictability for a given month. The stark changes in forced response, internal variability, and thus signal-to-noise across an ENSO season indicate that subseasonal fields should be used to diagnose potential predictability over North America associated with ENSO teleconnections. Using surface air temperature and precipitation as examples, this study provides motivation to pursue ''windows of forecast opportunity'' in which statistical skill can be developed, tested, and leveraged to determine times and regions in which this skill may be elevated.

KEYWORDS: Pacific-North American pattern/oscillation; Planetary waves; Rossby waves; Climate prediction; Probability forecasts/models/distribution; Statistical forecasting

1. Introduction

El Niño–Southern Oscillation (ENSO) is the most influential mode of global climate variability. ENSO usually develops during early boreal summer, peaks in winter, and decays in spring. Eastern Pacific tropical SST anomalies associated with ENSO events result in anomalous convective tropical precipitation. The latent heating response in the tropical Pacific drives divergent wind and vorticity anomalies in the upper troposphere, which communicate with the extratropics via Rossby waves. Due to the location of the extratropical divergence and the Asian–Pacific jet, quasi-stationary Rossby wave generation arises in preferred locations over the Pacific Basin (Wallace and Gutzler 1981; Sardeshmukh and Hoskins 1988; Bjerknes 1969), anchoring geopotential height (GPH) anomalies, and influencing North American weather, largely through the well-studied Pacific–North American (PNA) pattern (Bjerknes 1969; Wallace and Gutzler 1981; Trenberth et al. 1998).

Atmospheric general circulation models (AGCMs) are useful for examining the effect of ENSO on the predictability of the extratropical atmosphere (e.g., Lau and Nath 1996; Yang et al. 1998; Zheng et al. 2004; Matsumura et al. 2010; Branstator and Teng 2017). Ensemble members, influenced by similar lower boundary conditions but with perturbed initial conditions, result in a myriad of climate realizations that span the realistic range of atmospheric responses to boundary condition forcing. Lower-boundary forced signals manifest in the ensemble mean, working to make coherent anomalies despite the interensemble member variability. However, the precise extratropical response to ENSO is difficult to determine as 1) there is year-to-year SST variability among ENSO events (e.g., Deser and Wallace 1987; Newman et al. 2011; Johnson 2013) resulting in an array of forced atmospheric responses (e.g., Barsugli and Sardeshmukh 2002; Johnson and Kosaka 2016) and 2) it exists within a background natural climate variability, which acts to mask the SST forcing.

If the response to lower-boundary forcing is understood, then diagnosing and understanding the slow varying modes inherent to the land and sea surfaces (i.e., ENSO, seasonal snowpack, etc.) can aid in subseasonal-to-seasonal (S2S) predictions. Predictability is typically studied in a signal-to-noise ratio (SN) framework, in which the influence of the forcing is set in ratio against natural variability. SN has been used in several previous studies to diagnose the predictability of ENSO-driven cold-season extratropical circulation (e.g., Kumar and Hoerling 1998; Sardeshmukh et al. 2000; Peng and Kumar 2005; Abid et al. 2015). The SN can be increased via two pathways: 1) an increase in the influence of the forced component (e.g., as prescribed by the influence of ENSO SST and

Supplemental information related to this paper is available at the Journals Online website: https://doi.org/10.1175/JCLI-D-20-0391.s1.

Corresponding author: William E. Chapman, wchapman@ucsd.edu

DOI: 10.1175/JCLI-D-20-0391.1

atmospheric teleconnections) and 2) a significant decrease in atmospheric internal variability.

Many studies have demonstrated that the forced atmospheric response to interannual SST variations is important for the interannual variations in midlatitude climates despite internal variability (e.g., Shukla and Wallace 1983; Kumar and Hoerling 1995; Trenberth et al. 1998; Chen and Kumar 2015; Kamae et al. 2017). Additionally, there is consensus that an increased atmospheric forced component associated with ENSO (dominantly in the warm phase) events leads to a higher seasonal predictability within the PNA region (e.g., Kumar and Hoerling 1998; Chen and van den Dool 1999; Sardeshmukh et al. 2000; Peng and Kumar 2005; Abid et al. 2015) and over the North Atlantic (e.g., Honda et al. 2005; Jiménez-Esteve and Domeisen 2018; Ayarzagüena et al. 2018). However, studies disagree on the magnitude of ENSO modulation on internal atmospheric variability. Sardeshmukh et al. (2000) show an increased (decreased) extratropical internal variability during El Niño (La Niña). Others observed negligible changes in the internal variability of GPH (Kumar and Hoerling 1998) or associated surface variables (Chen and Kumar 2015) conditioned on ENSO state. Kumar et al. (2000) documented a nonlinear ENSO modulation of internal atmospheric variability in the PNA region, with El Niño decreasing extratropical 500-hPa GPH internal variability over the North Pacific greater than La Niña increased internal variability. However, this did not significantly improve SN relative to the contribution of the ensemble mean shift. Abid et al. (2015) and Peng and Kumar (2005) both report significant decreases (increases) in internal variability in El Niño (La Niña), leading to a significantly enhanced (diminished) SN relationship. However, there is evidence that these different conclusions may be due to the inclusion of different ENSO events and the number of examined ensembles, as SN does not vary wildly between models (Kang and Shukla 2006; Kang et al. 2011).

Trenberth et al. (1998) review studies that have diagnosed tropical–extratropical interactions due to anomalous tropical SSTs, and reveal key factors in determining the extratropical response. These include the location and intensity of tropical circulation anomalies, the effects of the mean flow on planetary wave propagation and forcing, interactions with midlatitude storm tracks, and interference from the internal chaotic variability of the midlatitude circulation (Trenberth et al. 1998, and references therein). The extratropical atmosphere has been observed to respond nonlinearly to ENSO cold and warm events, with a dominant SST forced response occurring in the warm phase and a milder reaction during cold events (e.g., Hoerling et al. 1997; Jiménez-Esteve and Domeisen 2019). Additionally, the impact of the annual cycle on the global wind field, and thus the barotropic Rossby waveguide, leads to drastic dynamic changes in the background state upon on which low-frequency forcing acts (Seager et al. 2010; Souders et al. 2014). Therefore, studies that examine the departure from seasonal means rather than incorporating important month-to-month differences are less effective and potentially misleading, particularly in late winter early spring (Newman and Sardeshmukh 1998). There has a been a recent re-examination of ENSO teleconnection and their extratropical manifestations (e.g., Zhang et al. 2014; Chen and Kumar 2015; Deser et al. 2017, 2018). However, there has been much less work that resolves the significant intraseasonal differences sparking from a changing monthly background state.

Increasing computational resources enable AGCMs to now run at higher resolution, with larger ensemble sizes, and to utilize longer historical records. These added statistics permit a reexamination and further exploration of large-scale dynamics and their influence on extratropical predictability from a SN standpoint. In this study, we test the reliability of the PNA-like response, and the effects on temperature and precipitation anomalies associated with ENSO events. We employ a high-resolution, large ensemble AGCM to examine the dynamic effect of anomalous ENSO forcing, and the seasonal variations at monthly resolution. We then explore noticeable differences in month-to-month internal variability driven by changes in large-scale dynamics within the PNA sector. The resulting monthly changes in SN relationships imply important changes in the level of predictability of given variables. Finally, to test the utility of the PNA driven changes, we diagnose whether the SN modulation manifests in monthly observed anomaly composites and also to improved predictive utility on monthly time scales. Utilizing in situ observations, we construct a simple probabilistic framework and adopt an information theory based potential predictability (PP) perspective (Kleeman 2002) to show the month-to-month impact of ENSO on temperature predictability.

2. Data and methods

a. AGCM experiments

To diagnose the atmospheric response to prescribed SST conditions, we utilize monthly mean values from a 100-member ensemble AGCM. Ensemble data were produced by the Meteorological Research Institute (MRI) AGCM, version 3.2 (Mizuta et al. 2012) at a horizontal spectral resolution with triangular truncation at wavenumber 319 and linear Gaussian grid (TL319; equivalent to 60-km mesh) with 64 vertical layers (Murakami et al. 2012). The AGCM was driven by observation-based SST, sea ice concentration, and radiative forcing (greenhouse gases, aerosols, and ozone) from 1951 to 2010, derived from the Centennial In Situ Observation-Based Estimates (COBE/COBE-SST2) (Hirahara et al. 2014). Small SST perturbations based on slight adjustments to the empirical orthogonal functions of the interannual variation of SST analysis [see the appendix of Mizuta et al. (2017)] were added to the COBE SST to account for uncertainties in analysis (Hirahara et al. 2014). It has been shown that the spread in climate response due to the perturbed SST is comparable to that due to initial condition perturbations (Mizuta et al. 2017). Sea ice concentration was derived from a quadratic equation on the sea ice/SST relationship (Hirahara et al. 2014). This dataset, titled the Database for Probabilistic Description of Future Climate Change (d4PDF), has been used to evaluate historical variations of atmospheric responses to global SST variability (e.g., Kamae et al. 2017; Mei et al. 2019; Naoi et al. 2020). More details of the experimental setup can be found in Mizuta et al. (2017) and Kamae et al. (2017).

TABLE 1. The d4PDF defined ENSO states by year.

	El Niño	La Niña	Neutral
Condition	DJF ONI > 1 K	DJF ONI < −1 K	1 K < DJF ONI > −1 K
Year	1957/58, 1965/66, 1968/69, 1972/73, 1982/83, 1986/87, 1991/92, 1994/95, 1997/98, 2009/10	1955/56, 1970/71, 1973/74, 1975/76, 1984/85, 1988/89, 1998/99, 1999/2000, 2007/08	Remaining

Kang et al. (2011) showed that synoptic transients in the Pacific basin comprise a large fraction of the signal and noise associated with the PNA. The high resolution of d4PDF, a state-of-the-art model with a physically consistent Northern Hemisphere atmospheric response to slowly varying mode forcing (e.g., ENSO, Pacific decadal oscillation, etc.) (Kamae et al. 2017) will likely represent transients (Hertwig et al. 2015), the atmospheric response to ENSO (Dawson et al. 2011), midlatitude blocking (Davini et al. 2017), and major weather regimes (Dawson and Palmer 2015) better than a low-resolution model as shown by previous studies referenced here.

b. Definition of ENSO and compositing

We define the ENSO index as the 3-month running mean of COBE-SST2 anomalies in the Niño-3.4 region (5°S–5°N, 170°–120°W). Anomalies are derived from centered 30-yr base periods updated every five years, in the exact manner as NOAA's oceanic Niño index (ONI). Years are classified as El Niño (La Niña) based on a December–February (DJF) value greater (less) than 1 K (−1 K) and a February–April (FMA) value greater (less) than 0.5 K (−0.5 K). These criteria result in 10 El Niño and 9 La Niña years. Table 1 specifies the categorical state of each year. We note that 8 of the 10 examined El Niño events fall into the category defined in Johnson and Kosaka (2016) that exceed the convective threshold in the eastern Pacific [~0.7-K December–March (DJFM) average SST anomaly in the region 5°S–5°N, 160°–120°W]. Diagnoses of nonlinear responses between El Niño and La Niña states are performed by regressing variables on contemporaneous COBE-SST2 monthly anomalies in the Niño-3.4 region for each state (El Niño/La Niña) independently, and examination of the slope of the fit. All values are demeaned (base period 1951–2010) and linearly detrended prior to the regression.

We examine monthly values for every model field. Temporal resolution is set at one-month intervals to focus on the intraseasonal dynamical atmospheric response to ENSO events. As El Niño's effects are largely pronounced in boreal winter (Philander 1989) and SST anomaly peaks in early winter (Neelin et al. 2000), we focus on November–April. We examine only monthly anomaly fields. For demonstrative purposes, in a few instances, the figures show an anomaly as well as the background climatology; these exceptions will always be indicated in the figure caption. We compute monthly anomalies, for every field, by subtracting the climatology, derived from the monthly mean using the base period 1951–2010. We then linearly detrend each time series to reduce potential effects of secular climate change. El Niño/La Niña composites are formed by averaging the monthly anomalies of the years defined in Table 1.

When testing significance on ensemble mean fields, we utilize bootstrap methods by resampling all of the ensemble mean monthly anomaly years in the record 1000 times and examine the 5th and 95th percentiles from the synthetic distribution. When examining the observational record, we utilize the composite and sampling methods described in Deser et al. (2017), where ENSO events are treated as exchangeable and uncertainty in the composite mean is determined by random sampling with resampling, again we sample the events 1000 times to determine confidence intervals.

c. Variable selection

We examine the Northern Hemisphere ENSO response on upper-level and surface variables. The 200-hPa GPH and wind anomalies are examined. The 200-hPa GPH is associated with strong teleconnection modes (Mo and Livezey 1986) between the tropics and the extratropics via changes in the large-scale atmospheric circulation in the Pacific–American and Atlantic–European sectors. The 200-hPa wind field, particularly in the Pacific jet region, undergoes a seasonal extension and intensification through early winter (November–January) as the Northern Hemisphere midlatitude baroclinicity increases, reaching its greatest zonal extent in February, and then retracts and weakens through March and the early spring (see Fig. 1 of Newman and Sardeshmukh 1998). Additionally, the 200-hPa zonal winds are modulated in El Niño (La Niña) winter with a southward (northward) shift, intensification (reduction) in magnitude, and thus an increased (decreased) zonal extent [see vector anomalies in Fig. 1 herein; see also Fig. 7 of Jiménez-Esteve and Domeisen (2018)].

We examine 2-m temperature (T2m) and precipitation, which are directly linked to the above mentioned 200-hPa GPH and wind fields. During El Niño years anomalous southerly winds advect warm marine air over northwestern North America while anomalous northerlies bring cooler continental air masses to the southeastern United States. A strengthened storm track increases precipitation over much of the southwestern United States, while leaving the northwestern United States anomalously dry. We observe the opposite relationship for La Niña seasons (e.g., Ropelewski and Halpert 1986; Dai and Wigley 2000; Jong et al. 2016; Deser et al. 2018, and many others). We are motivated to study these surface variables, in tandem with upper-level dynamics, in order to improve ENSO based S2S forecasting accuracy, which benefits vast swaths of North America's populations.

d. Observations

Observed 200-hPa GPH anomalies are derived from monthly data from the National Centers for Environmental

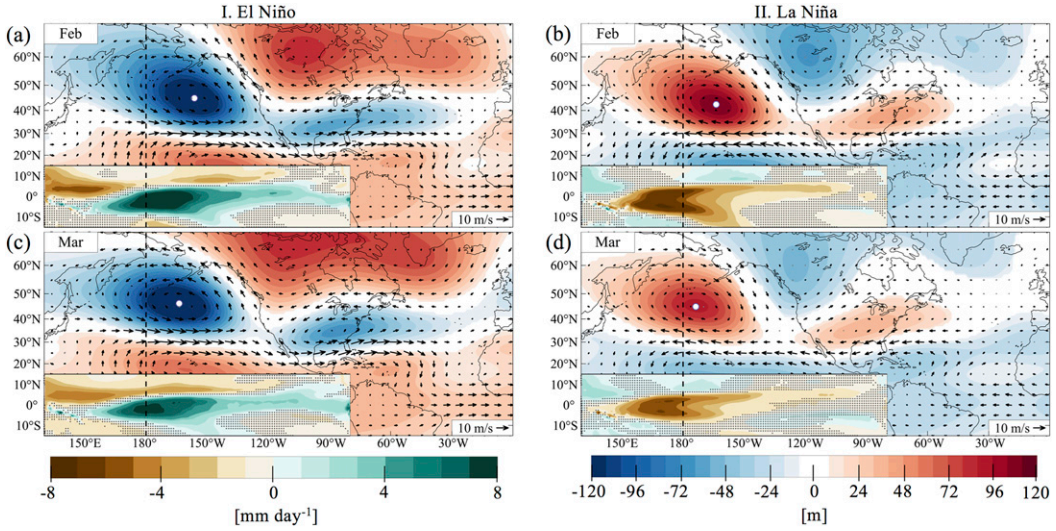

FIG. 1. February and March ensemble mean monthly response to (column I) El Niño and (column II) La Niña: composites of anomalous mean 200-hPa geopotential height (colorfill), 200-hPa winds (vector), and tropical precipitation (inset 15°S–15°N, 130°E–80°W) for El Niño and La Niña. Anomalous geopotential height and black wind vectors are shown for significant locations. Insignificant wind vectors are shown in gray. Insignificant tropical precipitation is stippled. Significant confidence intervals are determined by bootstrap, with resampling across all years 1000 times, and examination of the 5th and 95th percentile of the synthetic distribution. The white dot shows the Aleutian low center of action.

Prediction (NCEP)–National Center for Atmospheric Research (NCAR) reanalysis (Kalnay et al. 1996) available on a 2.5° × 2.5° grid. Daily average T2m data are utilized from the NCEP surface Gaussian product, which is available on the native T-62 Gaussian grid (approximately 1.875° × 1.875°) over North America (Kalnay et al. 1996). Finally, monthly observed precipitation is obtained from NOAA's precipitation reconstruction over land dataset interpolated onto a 1° × 1° grid (Chen et al. 2002). Every observed dataset spans years 1951–2019. All the datasets were downloaded from www.esrl.noaa.gov/psd/.

e. Rossby wave source and wave activity flux

We examine the 200-hPa Rossby wave source (RWS) (Sardeshmukh and Hoskins 1988):

$$\mathrm{RWS} = -\zeta_a D - \overline{v_\chi} \cdot \nabla \zeta_a . \tag{1}$$

The RWS is derived from the barotropic vorticity equation and locates vorticity forcing. RWS is computed using the magnitudes of the divergence D, the absolute vorticity ζ_a, and the irrotational component of the wind $\overline{v_\chi}$. The RWS can be decomposed to 1) $-\zeta_a D$, a vortex stretching term, representing the effects of divergence on vorticity change, and 2) $\overline{v_\chi} \cdot \nabla \zeta_a$, the absolute vorticity advection by divergent flow, provided by regions of strong vorticity gradient (i.e., subtropical jet). To compute RWS terms we use the windpharms Python package (Dawson 2016).

Following Takaya and Nakamura (2001) we use the horizontal 200-hPa wave activity flux (WAF) to explore the stationary Rossby wave sources and wave propagation in the extratropics. WAF is independent of the wave phase and parallel to the local group velocity of stationary Rossby waves. Monthly anomalies are regarded as perturbations. The horizontal flux is given as

$$W = \frac{P\cos\phi}{2|\overline{U}|}\begin{cases} \dfrac{U}{a^2\cos^2\phi}(\psi_x'^2 + \psi'\psi'_{xx}) + \dfrac{V}{a^2\cos\phi}(\psi'_x\psi'_y - \psi'\psi'_{xy}) \\ \dfrac{U}{a^2\cos\phi}(\psi'_x\psi'_y - \psi'\psi'_{xy}) + \dfrac{V}{a^2}(\psi'^2_y + \psi'\psi'_{yy}) \end{cases}, \tag{2}$$

where P, U, V, ψ', and a are pressure (scaled by 1000 hPa), zonal climatological wind velocity, meridional climatological wind velocity, perturbation geostrophic streamfunction, and the radius of Earth, respectively. Subscript x denotes the longitudinal derivative $\partial/\partial\lambda$, y the latitudinal derivative $\partial/\partial\phi$, λ the longitude, and φ the latitude.

f. Variance patterns

To extract the leading patterns of variability, we perform empirical orthogonal function (EOF) decomposition on monthly anomaly 200-hPa GPH fields of the ensemble mean and the internal variability fields. Decomposition is performed on each calendar month independently, and the full ensemble, and internal variability fields utilize all 100 members. All EOF patterns are area-weighted by the square root of the cosine (latitude), prior to decomposition. We express the orthogonal spatial fields as the pointwise regression of each time series on the one standard deviation change of the temporal principal component (PC) modes.

g. Signal-to-noise and potential predictability

With 100 ensemble members at 60-km resolution, d4PDF is unmatched in SN literature, and provides a more constrained estimate of the forcing. The deviation from the forced response, or ensemble spread, gives an approximation of the atmospherically derived internal variability.

We define context-dependent signal and noise as anomalies from the ensemble mean and spread, respectively, consistent with Kumar and Hoerling (1998). We note that the structure of atmospheric internal variability can, and in general does, depend on SST forcing. This dependence has been the subject of a number of papers (e.g., Sardeshmukh et al. 2000; Schubert et al. 2001; Abid et al. 2015). Strictly speaking, it is not valid to refer to internal variability simply as "noise," as this implies that it is independent of the forcing. However, for brevity we refer to SST independent internal variability as noise. We henceforth derive the climate signal, for any variable x, as the monthly mean anomaly of the ensemble mean state for individual months in a particular year (a) and ensemble members (i):

$$\overline{X_a} = \frac{1}{100}\sum_{i=1}^{100} X_{ia}. \tag{3}$$

The internal variability of the system is what remains in each ensemble, after removing the forced signal. Deviation from the ensemble mean [Eq. (4)] represents the variability of the atmosphere determined by any perturbation unassociated with the lower boundary condition and radiative forcing:

$$\overline{Y_a} = \frac{1}{100}\sum_{i=1}^{100} (X_{ia} - \overline{X_a})^2. \tag{4}$$

Spatially averaged (denoted by $\langle\rangle$) signal and noise root-mean-square (RMS) terms are defined as $\langle \overline{X_a}^2 \rangle^{1/2}$ and $\langle \overline{Y_a} \rangle^{1/2}$ respectively with SN being a representation of the ratio of the aforementioned terms (SN = $\langle \overline{X_a}^2 \rangle^{1/2} / \langle \overline{Y_a} \rangle^{1/2}$). This is analogous to the conventional assessment of potential predictability derived from standard ratio of variance analyses (Chervin 1986; Kumar and Hoerling 1995; Rowell 1998). SN is positive, and values greater than 1 imply that signal is greater than noise. Grid point RMS is area-weighted by the square root of the cosine(latitude) for spatially averaged fields.

h. Kullback–Leibler divergence

To help verify the AGCM findings on observations, we utilize the Kullback–Leibler (KL) divergence to assess the potential predictability of a conditioned distribution against climatology.

$$\mathrm{KL} = \sum_{i=1}^{I} (p_i) \log_2 \left(\frac{p_i}{q_i} \right). \tag{5}$$

The KL divergence is borrowed from information theory and measures (in units of bits) the extent to which a distribution q can be discerned from p (Kullback 1997). Here, since p and q are the conditioned and climatological distributions, respectively, the KL divergence can be interpreted as the extent to which a particular condition (i.e., Niño-3.4 > 1 K) informs the model prediction beyond climatology alone. Formally, it measures the number of excess bits needed to represent the examined variable when the condition is ignored (MacKay 2003; Cover and Thomas 2006).

The use of the KL divergence for assessing the PP of a forecast was proposed by Kleeman (2002). It has also been used to evaluate the potential forecast skill for multiple atmospheric variables (e.g., DelSole 2004; Roulston and Smith 2002) and to evaluate the effect of ENSO on North American T2m (Schamberg et al. 2020). In our analysis i will represent categorical anomaly states of below normal, normal, and above normal ($i \in \{1, 2, 3\}$), using the 33rd and 66th percentiles to quantize these states. Confidence intervals are determined by bootstrap with resampling all years in the record 1000 times and examine the 5th and 95th percentile from the synthetic distribution.

3. Atmospheric response to ENSO

It is important to note that the following results are reflective of the AGCM chosen for this analysis, and the ENSO event selection criteria. The sensitivity and response to SST forcing vary across individual models, resulting in varied ranges of internal variance and predictable ENSO forcing in the teleconnections. However, models with larger signals tend to have larger noise, making PP vary weakly across models (Kang and Shukla 2006).

During El Niño, the Pacific warm pool (and thus anomalous precipitation) shifts eastward. Forced by strong divergence at the upper levels in response to this precipitation, the Northern Hemisphere has a forced anomalous GPH response (Deser and Wallace 1990). Figure 1 shows the ensemble mean monthly composite of anomalous GPH in February and March by ENSO state. The leading mode of forced tropical precipitation (not shown) has a correlation to the Niño-3.4 index of 0.92 for the cold season [November–March (NDJFM); correlation on seasonal mean]. Anomalous tropical SSTs peak during December and fade through the remainder of winter and early spring. However, precipitation in the tropics is not controlled solely by SSTs, but modulated by the convective threshold (Gadgil et al. 1984; Graham and Barnett 1987; Johnson and Xie 2010). Due to higher climatological SSTs in combination with a retained El Niño SST signature in late winter and early spring, the upper-level divergence, and thus teleconnection, remains active well beyond the peak of tropical SST anomalies (Xie et al. 2018; Guo et al. 2019). Hoerling et al. (2001) credits the convective threshold as the source of a longitudinal shift in the North Pacific teleconnection between strong and weak ENSO events. The forced tropical precipitation response for every examined field peaks in February and remains anomalously strong into March. The extratropical GPH ENSO response is well studied, and a pressure pattern similar to the PNA emerges as a stationary Rossby wave (Wallace and Gutzler 1981). This PNA-like pattern is characterized by a deepened Aleutian low (AL), an increased Canadian high, and a deepened Florida low pattern extending into the Atlantic. A clear longitudinal shift is evident in the magnitude of the GPH anomaly in the late El Niño season (Figs. 1a and 1b, white dot;

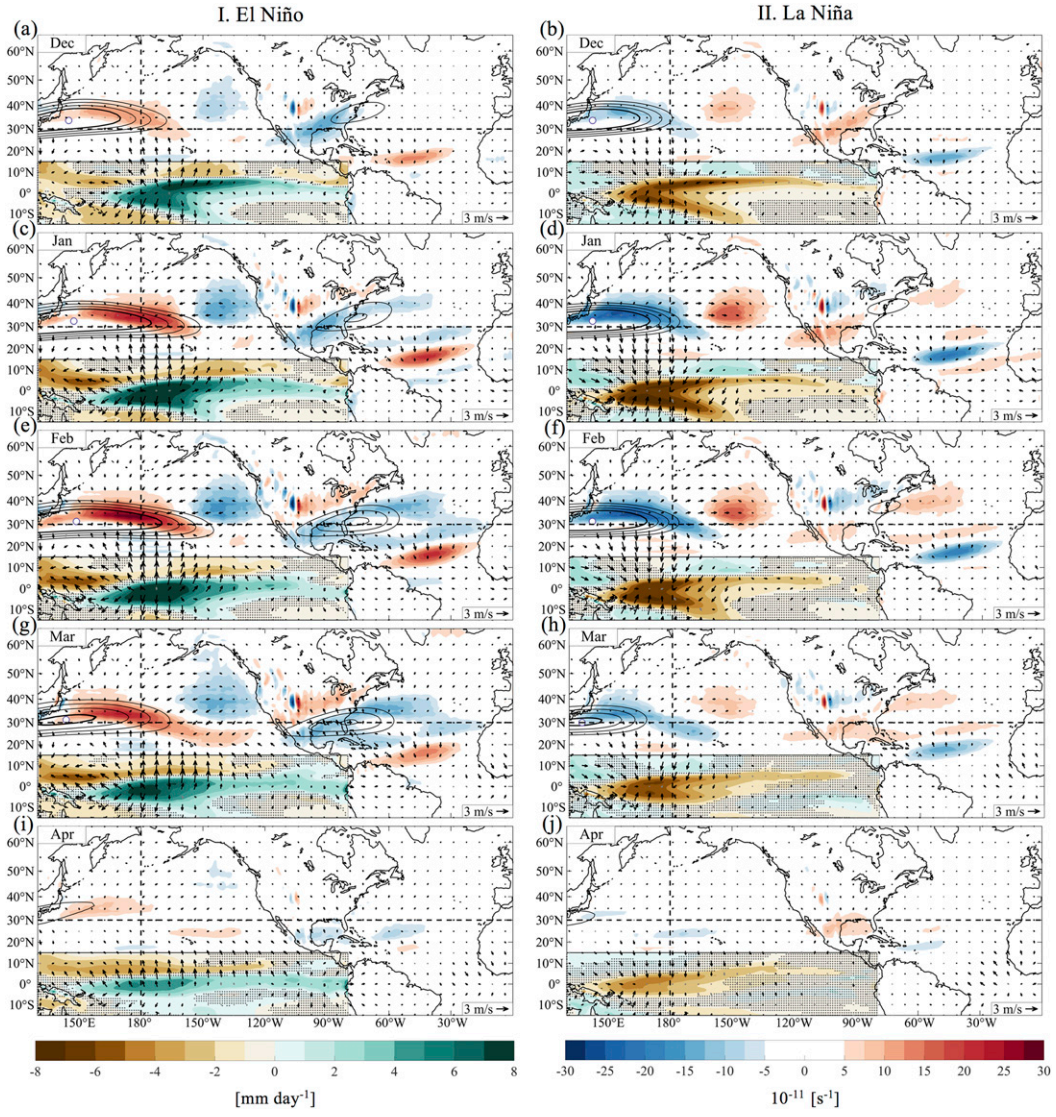

FIG. 2. Ensemble mean monthly (December–April) response to (column I) El Niño and (column II) La Niña: composite 200-hPa anomalies of Rossby wave source (colorfill), and anomalous divergent winds (vector), along with anomalous tropical precipitation (inset 15°S–15°N, 130°E–80°W) and 200-hPa zonal wind (climatology + anomalies; 45, 50, 55, and 60 m s^{-1} shown with black contours; 60 m s^{-1} is shown in bold). Significant Rossby wave source is shown. Insignificant anomalous tropical precipitation is stippled. Significant vectors are shown in black and insignificant in gray. Significant confidence intervals are determined by bootstrap, with resampling across all years 1000 times, and examination of the 5th and 95th percentiles of the synthetic distribution. The white dot shows the location of maximum 200-hPa zonal wind.

see also Fig. S1 in the online supplemental material for the full wintertime season anomalies). Additionally, the ENSO-forced North Atlantic response (Honda et al. 2001; Honda and Nakamura 2001) is not apparent until February/March, and shows a weaker anomalous response to ENSO forcing than the PNA. DJFMA ensemble mean monthly composites of anomalous GPH by ENSO state are shown in the supplemental material (Fig. S1).

ENSO anomalous upper-level winds are mostly geostrophic as evidenced by the 200-hPa anomalous wind vectors parallel to the 200-hPa GPH anomalies. The large-scale (synoptic) Pacific trough (ridge) is thus able to bring warm marine (cool polar) air into western North America, altering the surface temperatures (Zhou et al. 2014) during an El Niño (La Niña) event. Additionally, there is a distinct latitudinal shift in the subtropical jet (Fig. 2) that migrates from north to south (~5° as measured by the maximum zonal winds) throughout the ENSO season (Fig. 2). It is observed that due to the deepened (shallowed) Aleutian pressure anomaly, the jet stream is magnified (diminished), moves southward, and extends

(contracts) across the Pacific during El Niño (La Niña) (Norris 2000) (Figs. 1 and 2). This alters the longitudinal location of the jet exit region, the region of highest variability (Athanasiadis et al. 2010).

a. Rossby wave source

The ENSO RWS is depicted in Fig. 2. During El Niño (La Niña), anomalous divergence (convergence) is produced from deep tropical convection, with flow peaks at the edges of the heating region, resulting in anomalous convergent (divergent) regions in the subtropics. In the North Pacific, the position of the jet anchors the source term and often determines the major Rossby wave response of the North Pacific (Hakim 2003). Under the influence of the seasonal jet cycle, and the evolving ENSO precipitation signal (Fig. 2, inset), the peak response shifts east and west throughout the season, leading to a shifting center of action in the extratropical GPH response (Fig. 1, white dot). Interestingly, the teleconnection pattern shifts 7.5° (10°) from east to west alone between February and March of El Niño (La Niña) years, owing to the major contraction of the mean subtropical jet (Fig. 1). To first order, the monthly El Niño and La Niña response is symmetric, but the asymmetrical components, outside the strongest response regions, lead to important dynamic differences (Feng et al. 2017). The most notable asymmetry occurs in March when the El Niño composites show an extended positive RWS term that spans most of the Pacific while the RWS of the La Niña counterparts is relatively muted (Figs. 2g,h). Generally, asymmetry (in amplitude and position) is observed between the cold and warm composites, notably in the eastward shifted and amplified anomalous GPH and the Pacific extension of the RWS term (Figs. 1 and 2). Zhang et al. (2014) and Feng et al. (2017) have recently reexamined the asymmetrical components of the ENSO response and found they are driven by the background state of the atmosphere and play an important role in how ENSO affects the North American climate.

Figure 3 shows the forced RWS and its components for each ENSO category in the characteristic RWS anchoring region for boreal winter (Dawson et al. 2010; Nie et al. 2019), 25°–40°N, 145°E–155°W. We find a significant nonlinear RWS response to SST forcing between El Niño and La Niña seasons, with an increased sensitivity in El Niño periods (Fig. 3d). The nonlinearity is demonstrated by the slope of a linear fit calculated by regressing RWS on corresponding positive and negative Niño-3.4 anomalies (respectively) utilizing every monthly value in DJFM. The difference of these slopes is significant at the 10% level. We find no significant difference in the magnitude of the Niño-3.4 anomaly between El Niño/La Niña in any month over December–April (DJFMA; Fig. 3e). This nonlinear response to categorical ENSO states is a well-noted phenomenon (e.g., Hoerling et al. 1997, 2001; Hoerling and Kumar 2002; Johnson and Kosaka 2016; Jiménez-Esteve and Domeisen 2019; Trascasa-Castro et al. 2019), although the exact source of the nonlinearity in the extratropics is still subject to debate (Frauen et al. 2014). Many studies point to the convective precipitation response to tropical SST as a contributing factor (e.g., Hoerling et al. 2001; Chung and Power 2015). We find the observed RWS nonlinearity is alleviated somewhat (but remains significantly different) when regressing the RWS on tropical precipitation (not shown). The nonlinear response is seen in the magnitude of difference in the vortex stretching term for either ENSO state. The anomaly difference of the RWS term for cold and warm states is greatest in March, where both ζ_a and D remain highly anomalous in the warm phase (Fig. 3c). For both phases of ENSO, the RWS anomaly peaks in February, with near equal magnitudes in January and March of El Niño years (Fig. 3c). The absolute vorticity advection opposes the vortex stretching term, thus weakening the total RWS in DJF. However, the magnitude of $\overline{v_\chi} \cdot \nabla\zeta_a$ decreases back to climatology in March, diminishing the March RWS drop from the February RWS peak (Figs. 3b,c). April sees a nearly full decay of the RWS. We observe an asymmetric ENSO response in every examined monthly ensemble mean anomaly variable (GPH, RWS, divergent wind, etc.).

b. Wave activity flux

WAF is diagnosed using Eq. (2) to explore month-to-month Rossby wave propagation. Figure 4 shows the forced monthly composites of ENSO WAF (vector), the anomalous 200-hPa GPH (colorfill), and the anomalous RWS (contour). In both ENSO states, WAF emanates from the strong RWS at the exit of the Pacific jet through the Aleutian low (AL) toward North America. The December El Niño Canadian limb of the teleconnection pattern shows a stronger anomalous signal than the corresponding Niña composite. By January in the El Niño season a canonical wave train has emerged, with the classic four-pole PNA pattern. The January La Niña composite shows a strong AL signal but mostly insignificant WAF over land. WAF peaks in February, with a fully developed wave train pattern in both ENSO phases. This corresponds with the strongest PNA-like anomaly GPH pattern. The maximum Florida limb of the teleconnection pattern, for both WAF and GPH anomalies, is observed in March of Niño seasons. The Niña pattern has diminished greatly by March and both WAF and GPH appear relatively weak in April. Across the season the WAF shows an extreme asymmetry between El Niño and La Niña, varying with the asymmetric GPH anomalies. Interestingly, the El Niño/La Niña pathways appear different in Rossby wave propagation for the Florida low GPH anomalies with El Niño WAF showing a more southerly route [consistent with Seager et al. (2010)].

The Icelandic low (IL; ~64°N, 30°W) undergoes a seasonal shift in phase expression between early [November–December (ND)] and late season [February–March (FM)] ENSO states. This is a well-studied shift that is robust in the observational record (e.g., King et al. 2018) although climate models typically do not represent the early season mechanism well (Ayarzagüena et al. 2018). The d4PDF captures the early-season IL anomalies in the ensemble mean (Figs. 4a,b), which stem from increased precipitation anomalies in the Gulf of Mexico leading to enhanced anomalous RWS at 250 hPa (Figs. 2a,b). A late-season emergence of an anomaly in the IL occurs in February/March of El Niño years. In February a wave train emanates as an extension of the PNA-like pattern, extending the Canadian high and Florida low into the Atlantic.

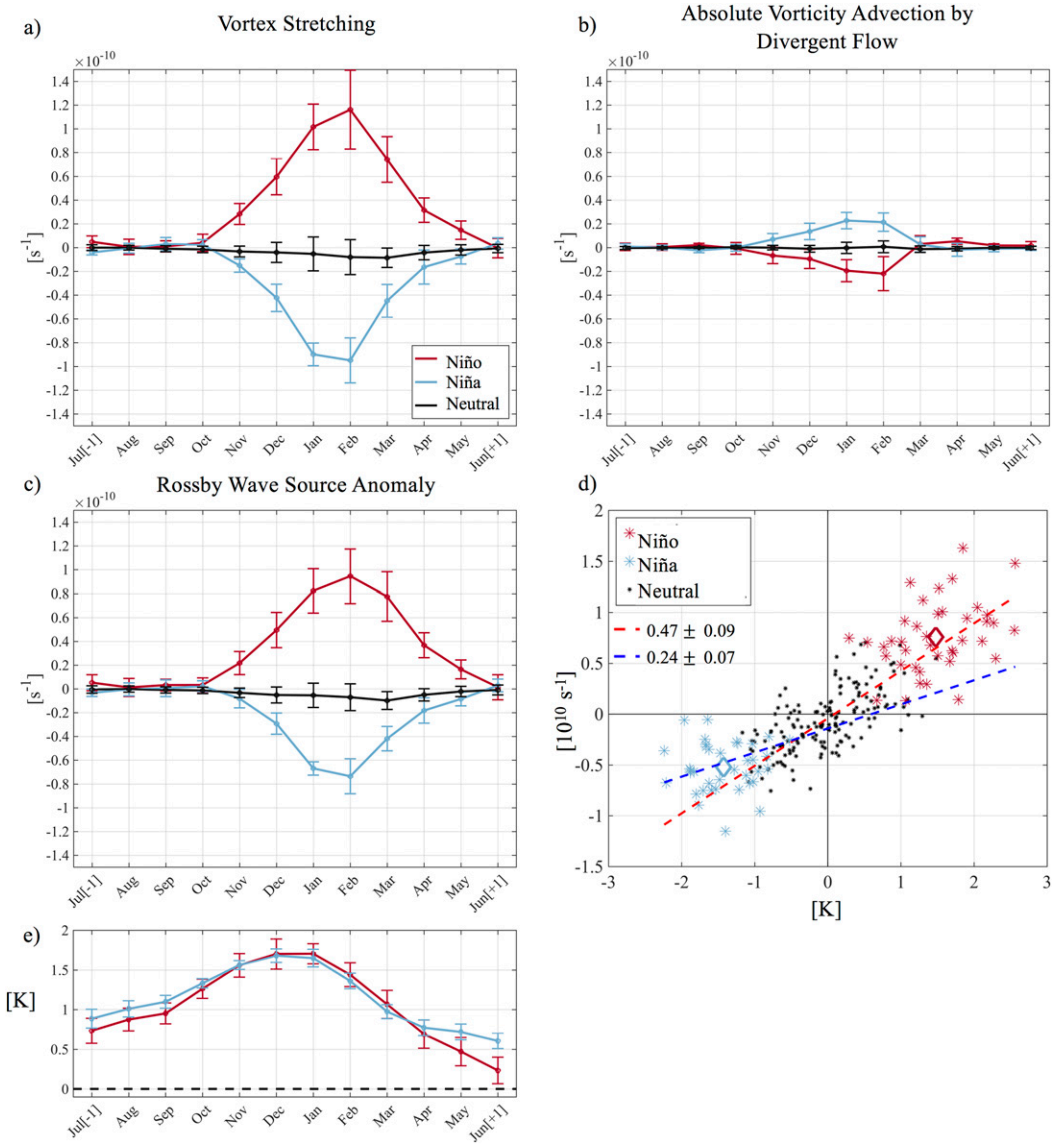

FIG. 3. (a) Vortex stretching (VS). (b) Absolute vorticity advection by divergent flow (AVA). (c) Rossby wave source (RWS) anomaly for El Niño (red line), neutral (black line), and La Niña (blue line) year (categorized in Table 1) composites. (d) Average RWS anomaly index with respect to the Niño-3.4 anomaly for individual months DJFM. Red (blue) markers indicate El Niño (La Niña) years. Diamond marker indicates the class (Niño/Niña) composite mean. The dashed red (blue) line indicates the linear fit calculated using every positive (negative) Niño-3.4 anomaly. The slope of each line is shown with 2σ uncertainty determined by bootstrap, with resampling across all years, 1000 times. (e) Composite El Niño and La Niña (negative) anomaly SST in the Niño-3.4 region for years specified in Table 1; 5th and 95th confidence intervals are shown, determined by bootstrap with resampling 1000 times. VS, AVA, and RWS are area averaged in the region 25°–40°N, 145°–155°W.

A large body of literature finds that the late season ENSO influence on the IL is due to changes in stratospheric circulation (Trascasa-Castro et al. 2019, and references therein). We observe an additional tropospheric pathway with significant RWS terms stemming from increased precipitation (precipitation anomaly not shown) in the Gulf of Mexico and Florida region interacting with the Atlantic jet, which is energized and extended in El Niño years (Figs. 2e,g). We see a particularly nonlinear RWS and WAF response between March of La Niña and El Niño years in this region, with El Niño leading to the shallowing of the surface IL anomalies, and the negative phase of the NAO. This late-season development of the IL and peaking of the Florida low PNA-like pattern was also observed in multiple studies and referred to as the Aleutian–Icelandic low seesaw index (AII) (e.g., Honda et al. 2001; Honda and Nakamura 2001; Honda et al. 2005).

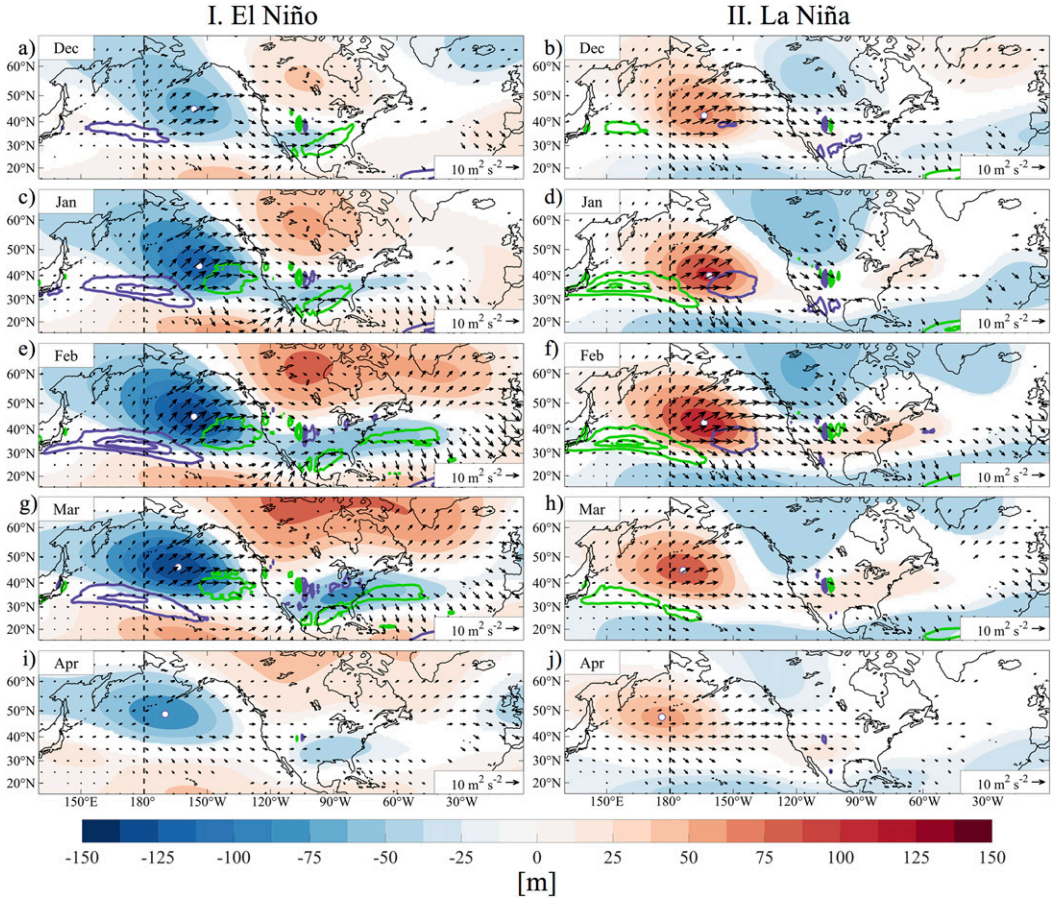

FIG. 4. Ensemble mean monthly (DJFMA) response to (column I) El Niño and (column II) La Niña: 200-hPa TN wave activity flux (WAF) composite (vector), 200-hPa geopotential height anomaly (colorfill), and anomalous Rossby wave source [contour; purple (positive), green (negative); intervals ± at 10, 20, and 25 × 10^{-11} s^{-1}]. Only significant geopotential height is shown. Significant WAF vectors are shown in black. Significant confidence intervals are determined by bootstrap, with resampling across all years 1000 times, and examination of the 5th and 95th percentiles of the synthetic distribution. White dot shows the Aleutian low center of action.

c. *Additional sources of ENSO-forced extratropical waves*

Although we focus on the dispersion of Rossby waves excited by tropical heating, extratropical waves are additionally generated and anchored due to barotropic energy conversion from the subtropical jet deceleration ($\delta\overline{U}/\delta x < 0$) in the jet exit region and synoptic-scale transient eddy vorticity fluxes. Both mechanisms are modulated by ENSO. Jet deceleration allows waves to effectively extract kinetic energy from the zonally asymmetric climatology, via an energy transfer from the climatological stationary eddies to the anomaly (Simmons et al. 1983; Branstator 1989, 1992; Feldstein 2002; Athanasiadis et al. 2010). The anomalous synoptic transient activity along the Pacific storm tracks—which is extended eastward to the jet exit region during El Niño years (Seager et al. 2010; Harnik et al. 2010)—produces the seasonal-mean transient eddy vorticity flux convergence anomalies that reinforce the local signals of seasonal-mean circulation anomalies (Held et al. 1988; Straus and Shukla 1997). Moreover, the downstream propagation of transient eddies from the Pacific to the Atlantic basin provides a tropospheric pathway for NAO-related GPH anomalies (Li and Lau 2012; Jiménez-Esteve and Domeisen 2018) during ENSO.

4. Signal versus noise

We examine the leading mode of variability in two categories: the internal variability and the forced response (Fig. 5, columns I and II, respectively). The leading mode of variability accounts for ~20%–30% (month dependent) of the full variability (not shown), and both internal variability and the forced response have loadings in the PNA regions. However, distinct differences are observed. Note that the internal variability (Fig. 5, column I) patterns have a far southward extent of the Canadian high pressure system that largely covers the western United States, and the forced response has a linked low pressure system between the AL and the Florida low (Fig. 5, column II). The forced pattern more closely resembles the El Niño composites (see loading locations of Fig. 4) and the anomaly strength in the principal component agrees with this finding (not shown).

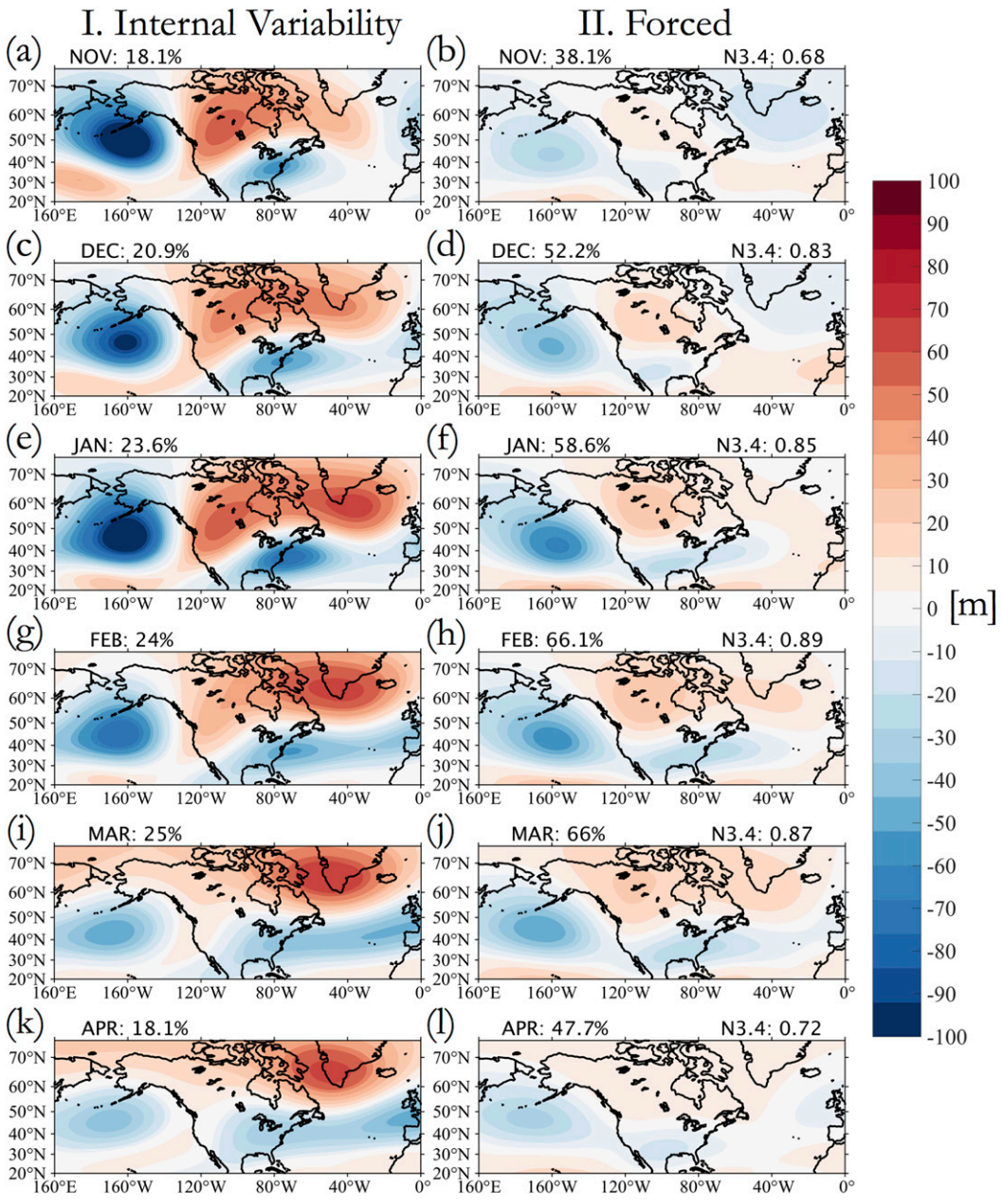

FIG. 5. (column I) Internal variability and (column II) forced leading EOF mode of 200-hPa atmospheric geopotential height variability, calculated for each month individually, with percentage variability explained by this mode, for each month, and the correlation of the principal component to the concurrent Niño-3.4 anomaly index (at top right). PCs are normalized to unit variance.

Although the NAO loadings are present in the internal signal throughout boreal winter, the forced negative NAO signal does not emerge until February. The NAO, with the exception of very low-frequency forcing signals, is not necessarily strongly forced by an oceanic mode (Stephenson et al. 2000). However, ENSO-forced PNA/NAO patterns/signatures can be spurred by the PNA's advection of air masses, which leads to baroclinic waves forming the North Atlantic storm track (Pinto et al. 2011). By this mechanism, a negative interannual correlation between the intensities of the Aleutian and the Icelandic lows reaches a value of ~ -0.7 between the indices averaged from February to mid-March in observations. (Honda et al. 2001; Orsolini et al. 2008). During February and March, the leading forced modes (Figs. 5h,j) show loadings consistent with a negative NAO phase (Barnston and Livezey 1987) that is correlated with the Niño-3.4 signal (Huang et al. 1998) and peaks in the late winter/early spring. There has been much work on the dispersive characteristics of climate models

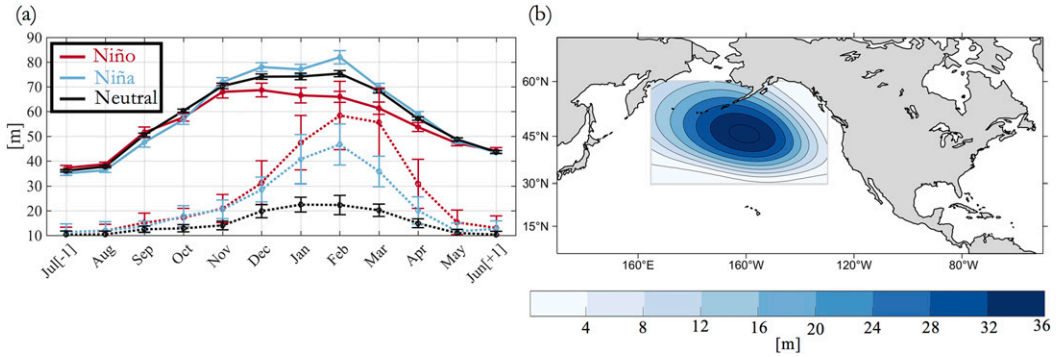

FIG. 6. (a) Yearly development of composite RMS signal (dotted line) and noise (solid line) area averaged in (b) the region of interest (30°–60°N, 165°E–130°W) for El Niño (red), La Niña (blue), and neutral (black) years, as defined in Table 1, for monthly values from 1951–2010. Error bars show the 5th and 95th percentile bounds determined by bootstrap with resampling 1000 times across all El Niño years. The leading mode of variance (DJFMA seasonal mean) in the region of interest in (b), PC is normalized to unit variance.

and seasonal-to-multiseasonal predictability of the NAO (e.g., Shi et al. 2015; Scaife and Smith 2018; Weisheimer et al. 2019). The NAO fraction of variance is low compared to the forced ensemble counterpart in every month. However, it has been observed that the NAO is more predictable (in a signal-to-noise framework) than climate models typically represent it to be (Scaife and Smith 2018; Siegert et al. 2016; Zhang and Kirtman 2019) and a model postprocessing variance adjustment (Smith et al. 2020) could show a more enhanced variance fraction of the full ensemble in the ensemble mean.

The leading mode pattern accounts for ~40%–70% of the forced response variance and its principal component correlates with the Niño-3.4 anomaly index at ~0.65–0.90, month dependent. The DJF average fraction of variance in the leading mode (~58%) agrees well with previous studies of ENSO forced variance [e.g., 53% (Kumar et al. 2005) or 56.2% (Zhang et al. 2016)]. However, the forced PNA-like pattern is particularly dominant in FM (~66% of variance) and correlates strongly with the Niño-3.4 index (~0.9).

a. ENSO modulations of internal variance

Motivated by the important role the AL plays in modulating North American weather (e.g., Gibson et al. 2020), 200-hPa GPH signal and noise (Fig. 6a) over the North Pacific (30°–60°N, 165°E–130°W) is diagnosed. Climatologically, GPH noise is greatest during boreal winter, peaks in February, and is lowest in summer (Fig. 6a, solid black line). Internal variability is significantly (although weakly) different from climatology in February of La Niña years (Fig. 6a, solid blue line). We find a modulation of the GPH noise conditioned on the ENSO state (Fig. 6a). With adjustments of up to ~10% (by percentage difference) of modulated RMS across DJFM (Fig. 6a) in El Niño. This is a similar finding (although ~7% less) than that of Abid et al. (2015) in El Niño years. Abid et al. (2015) attributed the modulation of noise in ENSO years to extratropical transients, and not to increased tropical precipitation variability [tropical variability, which is proportional to SST magnitude, increases (decreases) in El Niño (La Niña) years; Peng and Kumar 2005]. The forced AL peaks in February of El Niño years, diminishing slightly through March. Owing to decreased noise and increased signal in February and March, the regional SN approaches 1 in these months.

Figure 7 displays the FM ENSO spatial modulation of the internal variability via monthly composites of GPH RMS noise with climatological noise depicted in solid contours. ENSO modulation is most apparent in JFM, with a peak in February. Noise modulation becomes effective for PP in March of El Niño years, as noise climatologically decays in concert with an El Niño mean shift (Figs. 6a and 7, black contour). The internal variability is largely decreased (increased) during El Niño (La Niña), with the exception of the jet exit region, which is the highest source of variability in either ENSO state. The ENSO effect on internal variability is stronger in the warm phase than in the cool phase (cf. Figs. 7c and 7d). La Niña noise in the northwest Pacific is significantly increased in DJF, peaks in February, and decays back to climatology by March (Fig. 6a). Abid et al. (2015) found similar diminished noise in the extratropical PNA region during El Niño events. Abid et al. (2015) point to the noise intensification associated with barotropic instability in the PNA region as a possible driver (Simmons et al. 1983; Branstator 1985). Eastward (westward) extensions (contractions) of the zonal jet are collocated with decreased (increased) noise in the western Pacific and over the southern United States. The areas of increased (decreased) El Niño (La Niña) noise (~40°N, 150°W) are directly related to the shift in the Pacific jet exit region (Fig. 7). DJFMA ENSO spatial modulation of the internal variability via monthly composites is shown in the online supplemental material.

b. Signal-to-noise ratio

Using SN as a proxy for PP (Sardeshmukh et al. 2000), we examine 200-hPa GPH, T2m, and precipitation SN during ENSO events. Area-averaged SN for GPH, T2m, and precipitation is shown (Figs. 8a,b,c, respectively) in the PNA sector (defined here as 25°–70°N, 155°E–60°W). T2m SN is only accounted for over land. FMA GPH SN shows a significant difference between ENSO categories (Fig. 8a). Temperature and precipitation show a significant difference in March and April

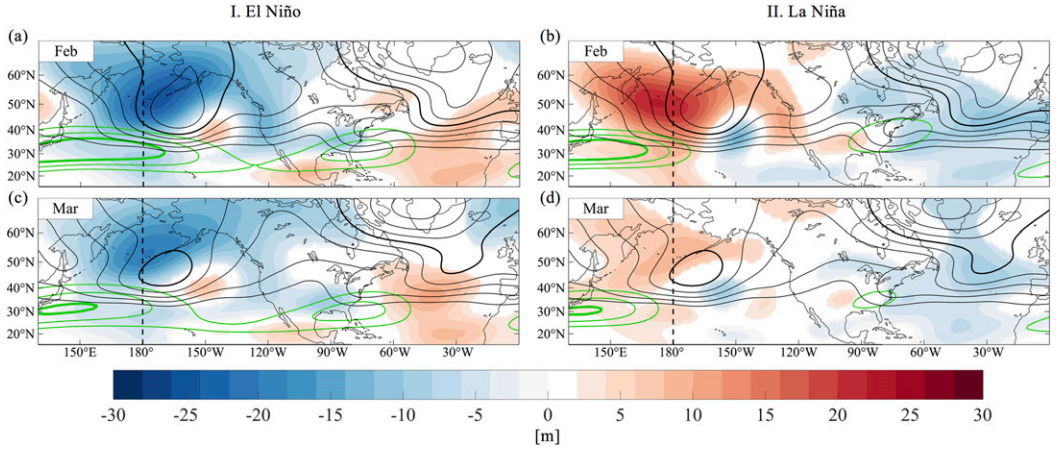

FIG. 7. February and March RMS noise response to (column I) El Niño and (column II) La Niña, with a composite map of anomalous RMS noise 200-hPa geopotential height (colorfill); values that are not significant are not shown. The climatology of RMS noise is shown in black contours (60, 70, 80, 90, 100, 110, and 120 m; 100 m shown as the bold contour). Composite zonal wind is in green contours [40, 50, and 60 m s^{-1} (climatology + anomalies), the 60 m s^{-1} contour is shown in bold]. Significant confidence intervals are determined by bootstrap, with resampling across all years 1000 times, and examination of the 5th and 95th percentile of the synthetic distribution.

(Fig. 8b). El Niño/La Niña precipitation is significantly different in March (Fig. 8c). We observe a statistically significant (10%) nonlinearity (diagnosed as described above) of month-to-month SN across all variables conditioned on the Niño-3.4 anomaly (Fig. 8d; T2m and precipitation not shown). Figure 9 shows the monthly composites of SN across North America for GPH and T2m. The teleconnection most dominantly affects T2m in El Niño in northwestern North America (NWNA), through the advection of warm marine air. The NWNA T2m SN increases in January, peaks in March, and remains elevated during April, shifting northward throughout the season. We theorize the April NWNA T2m SN to be a manifestation of a decreased snowpack from the previous month's warm temperature anomalies (Zhang et al. 2011). The American southeast T2m is also affected by the southernmost limb of the PNA pattern. Northern Mexico and Florida show the most consistent, and significant SN, which peaks in March of El Niño years. The temperature SN patterns match the Deser et al. (2018) observed and simulated ENSO anomaly seasonal composites well, but they occur in distinct months in boreal winter, rather than showing a full seasonal shift. This could indicate that averaging over a season acts to mute the forced ENSO signal. Additionally, La Niña SN is generally weaker in the T2m field, in agreement with diminished dynamic model forecast skill when compared to El Niño seasons (Chen et al. 2017).

GPH SN is greater over the PNA region, in EL Niño than La Niña, showing patterns that match the forcing signal (Fig. 4). Figure 10 shows the monthly composites of SN across North America for GPH and precipitation. La Niña SN only peaks in the southern half of the AL region (Figs. 10f, h), where internal variability is low (Fig. 7). GPH SN does not peak in the IL region, although in observations northern Canada and the eastern United States show a significant shift in temperature anomalies (see Deser et al. 2018). This is an indication that the northern limb of the PNA teleconnection response in d4PDF is potentially overdispersive.

We detected low precipitation SN across the ENSO seasons (Fig. 10). FM SN shows an emergent reflection of the well-studied meridional dipole of ENSO precipitation over western America (Dettinger et al. 1998). GPH patterns are often represented well (Flato et al. 2013), and an increased northern continental SN value in El Niño could be indicative of SST-forced anomalous GPH patterns steering precipitation events away from the NWNA to impact more southerly locations. The largest source of SN in both ENSO states is in the eastern Pacific (~30°N, 135°W), highlighted by Zhou et al. (2014), as enhanced (diminished) westerlies steer extratropical storms to a more southerly (northerly) position during El Niño (La Niña), causing increased (decreased) precipitation. Additionally, northern Mexico and Florida show a significant SN, magnified in La Niña years. Previous studies have shown significant influence of tropical SST anomalies on North American precipitation variability (e.g., Seager et al. 2005; Meehl and Hu 2006; Dai 2013; Burgman and Jang 2015). Accurately representing precipitation involves heavily parameterized processes, and linking to surface fields (topography, coastline, vegetation), making it difficult when compared to T2m representations.

5. ENSO potential predictability and observations

Using SN as a proxy for PP, we have demonstrated month-to-month ENSO-driven changes in GPH, T2m, and precipitation in the d4PDF model ensemble. We now verify these findings on observations. The following analysis is performed on all years shown in Table 1 and extended to include years (2010–19) that are beyond the d4PDF record. Apart from 2015/16 (El Niño) and 2010/11 (La Niña), every added year is ENSO neutral.

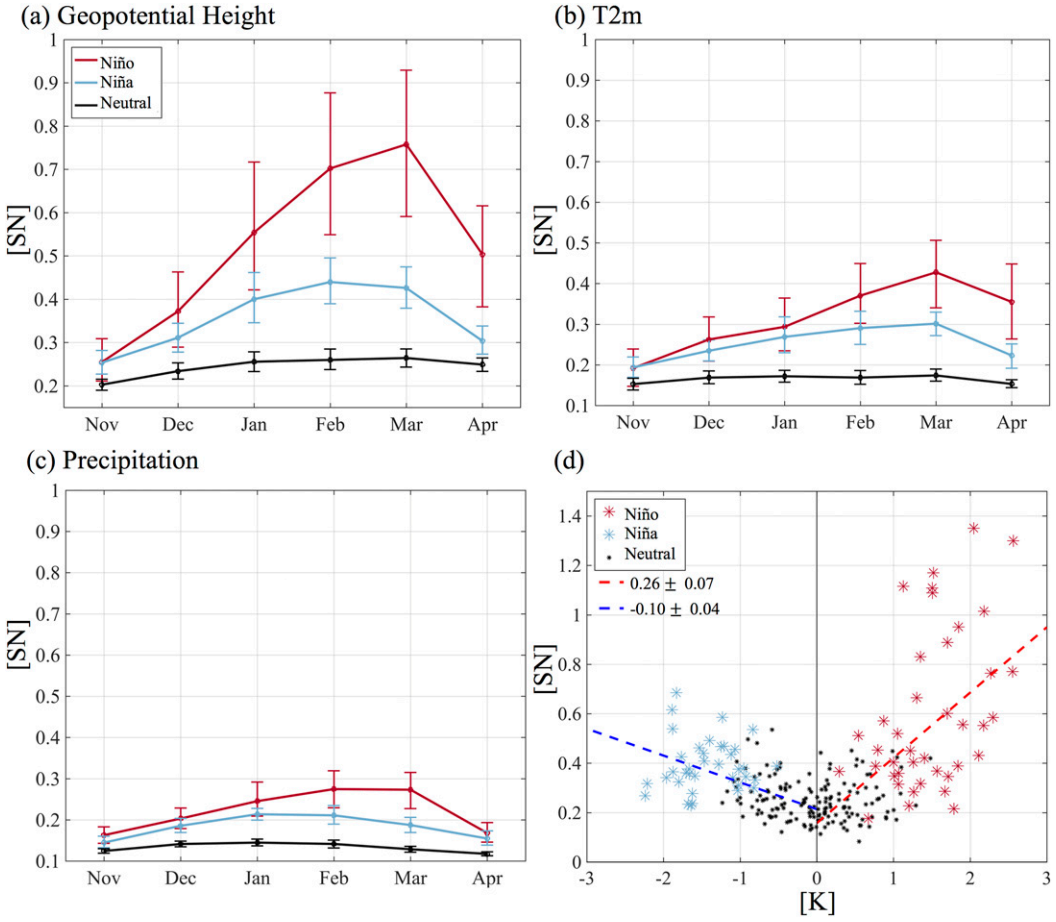

FIG. 8. Area averaged (25°–70°N, 155°E–60°W) signal-to-noise ratio for (a) 200-hPa geopotential height (b) 2-m temperature (values over land only), (c) precipitation, and (d) geopotential height SN with respect to the Niño-3.4 anomaly, calculated for individual months (DJFM only). Red (blue) markers indicate El Niño (La Niña) years. Dashed red (blue) line indicates the linear fit calculated using every positive (negative) Niño-3.4 anomaly. The slope of each line is shown with 2σ uncertainty. The 5th and 95th percentile confidence intervals are determined by bootstrap, with resampling across all years, 1000 times.

Figure 11 shows the d4PDF ensemble spread, d4PDF forced ensemble mean, observed composite mean, and every observed value of the PNA (Figs. 11a,b) and the AII (Figs. 11c,d). The PNA is defined at 200 hPa by the four-point index described in Wallace and Gutzler (1981) and is constructed using standardized anomaly time series at each point. The resulting index is normalized by the standard deviation of the combined DJF values. The AII is defined at 200 hPa in the characteristic regions described in Honda et al. (2005) and is calculated as the normalized anomalous IL intensity subtracted from the normalized anomalous AL intensity. Each index uses values from 1951 to 2010 (the d4PDF period of record) to form the normalization climatology. The model mean and spread in the PNA/AII match the observed values well. PNA composite mean displacement for d4PDF and observations both peak in March of El Niño years with a near-zero anomaly shift in November, December, and April. In agreement with the d4PDF, La Niña has a generally weaker mean shift and sits well within the d4PDF model spread. The La Niña signal fades in March/April. The AII observed mean sits well within the spread of the d4PDF model. Using the IL index alone gives a good fit between model spread and observations, but a dampened magnitude (not shown), compared to the AII.

Figure 12 shows the observed monthly composite of anomalous precipitation and 200-hPa GPH from December to April by ENSO state. We now list noticeable similarities between the observed monthly anomalies (Fig. 12) and the SN relationships displayed in Fig. 10. 1) The significant AL and Florida low GPH anomaly match nearly exactly for each ENSO state across the full season, and in La Niña the AL GPH composite is collocated with the low GPH noise anomaly shown in d4PDF (Fig. 7, column II; ~40°N, 150°W). 2) December shows very little GPH or precipitation anomaly signal especially affecting the North American west coast. 3) La Niña composites show less significant anomaly than the El Niño counterpart, in precipitation and GPH. 4) The Gulf of Mexico and Florida are

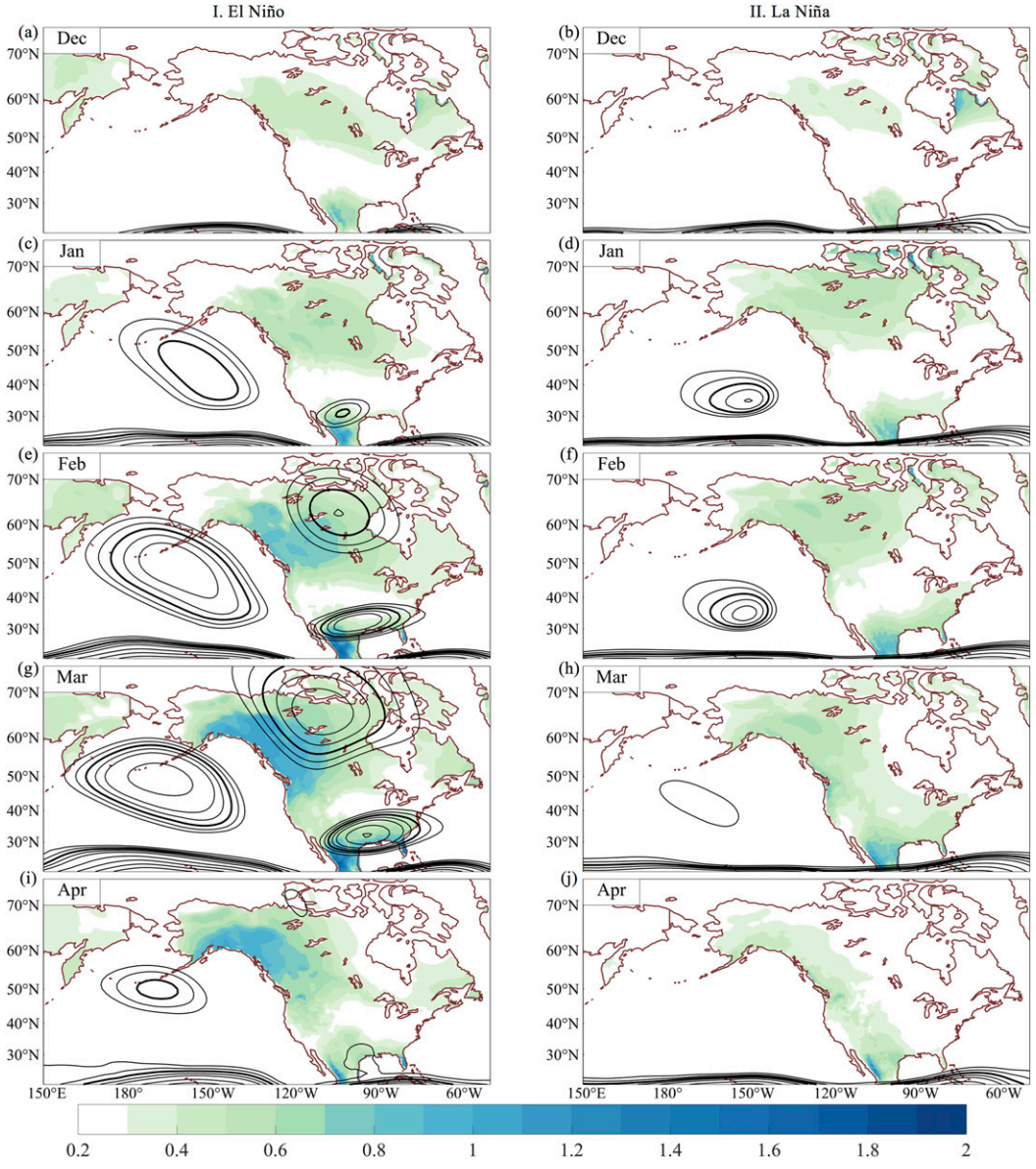

FIG. 9. Monthly (DJFMA) signal-to-noise relationship for temperature (colorfill) and 200-hPa geopotential height (contour, 0.2 intervals beginning at 0.6, with 1 shown as the bold contour) for (column I) El Niño and (column II) La Niña years (as defined in Table 1).

particularly attenuated in La Niña. 5) March El Niño precipitation extends farther into the continental United States. We note that specific months magnify specific anomaly loading locations throughout the ENSO season highlighted in the seasonal composite seen in Deser et al. (2017, 2018). For completeness, we show the same figure but for observed monthly temperature anomalies in the online supplemental material (Fig. S3).

The largest precipitation pattern discrepancy occurs in the western United States shown in JFM, which is shifted into the eastern Pacific in the d4PDF SN (Fig. 10 vs Fig. 12). Additionally, there is a clear model bias associated with the high-pressure limb of the PNA pattern in northeast Canada. This could be an indication of d4PDF overdispersiveness of the northern limb of the PNA pattern across the ensemble members, and a lack of forcing in the early season, which is consistent with the findings of Scaife and Smith (2018) and Smith et al. (2020) that the NAO is more predictable than climate models typically demonstrate.

To test the utility of the PNA-driven changes in SN on observations, we adopt an additional potential predictability metric developed from KL divergence (KLPP) to show the ENSO forcing on temperature predictability. We build distributions following the probabilistic framework in Johnson et al.

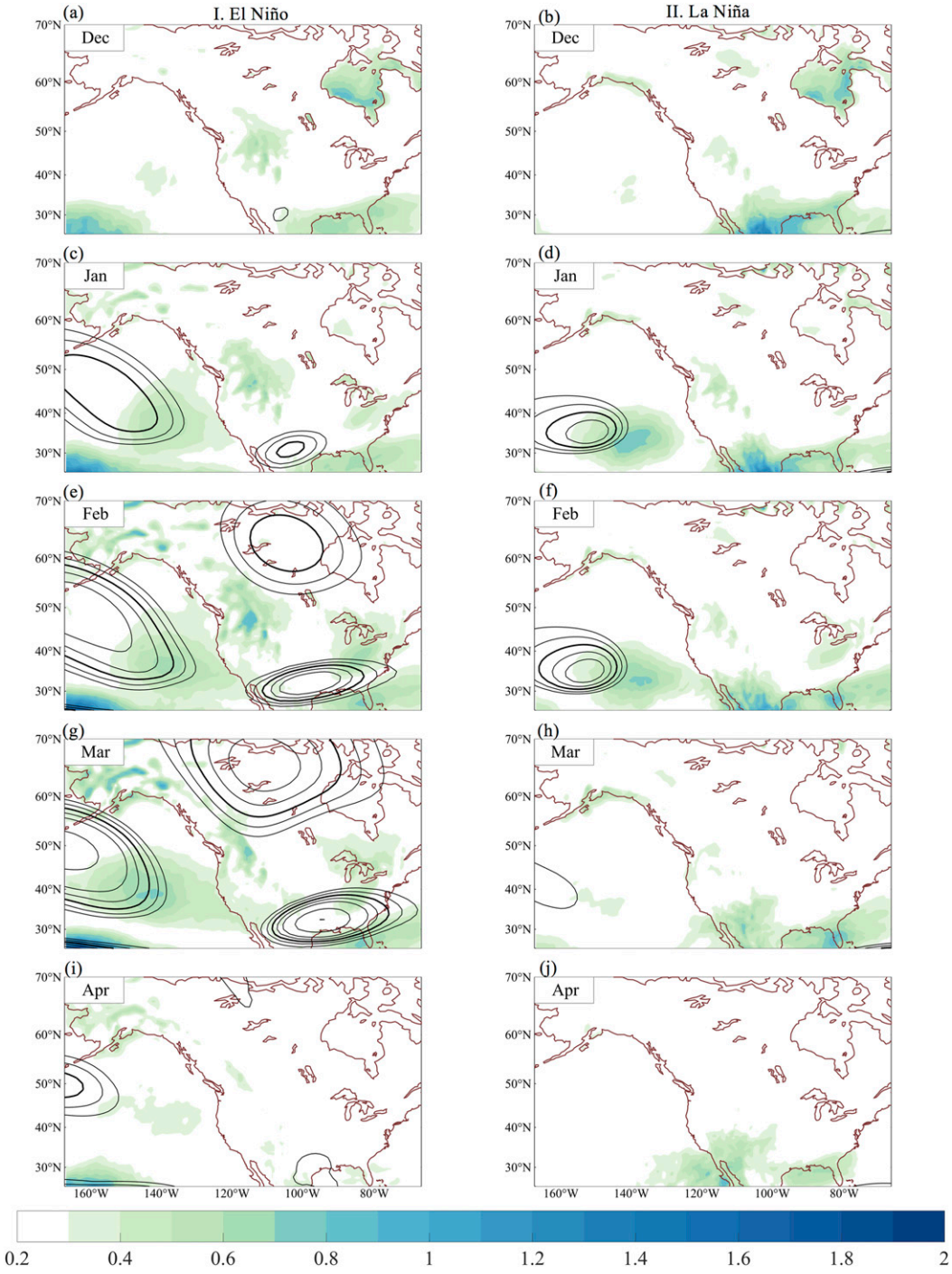

FIG. 10. As in Fig. 9, but for North American precipitation (colorfill) and 200-hPa geopotential height (contour)

(2014) and examine the T2m distributions for the weekly averaged temperature anomaly shifts conditioned on an ENSO state. These calculations are performed using observations, and not the d4PDF model. An observation is quantized into one of three divisions (below normal, normal, above normal), based on the highest probability tercile determined by the state of ENSO. The KL divergence is then computed [Eq. (5)]. We again show a monthly granularity to observe the evolution of potential forecast skill.

To illustrate, at every grid point we develop a climatological weekly temperature distribution across all years, using average weekly T2m observations. We use the 33rd and 66th percentiles

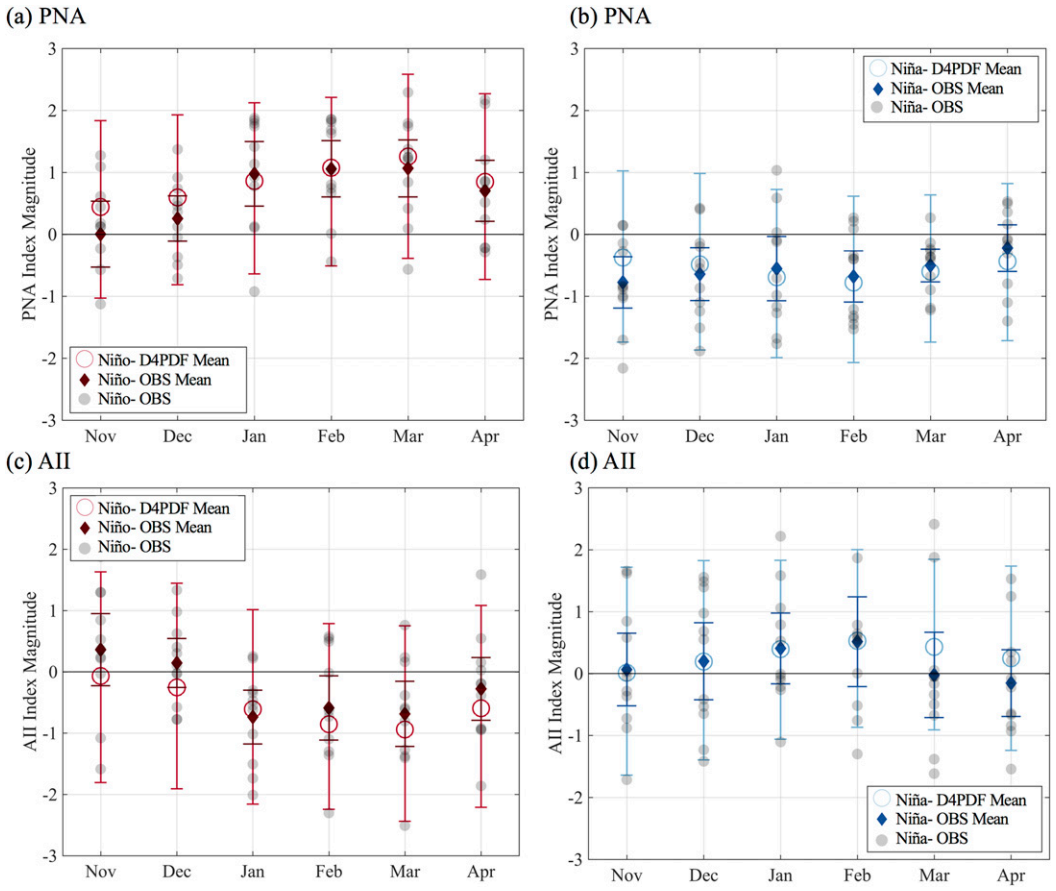

FIG. 11. Monthly d4PDF (a),(b) PNA index and (c),(d) AII index mean and 5th and 95th percentiles across 100 ensemble members (open circle) and for observations (diamond, showing observation composite mean from ENSO years; observed values shown in gray dot) for (left) El Niño and (right) La Niña years. The observation mean spread is estimated from bootstrap with resampling 1000 times across years. The d4PDF ensemble intervals are estimated from bootstrap with resampling 1000 times across all members.

to quantize the anomaly value into categorical states $T \in \{\text{below normal, normal, above normal}\}$. Therefore we have threshold values to divide anomalous temperature into equally probable categories ([P(below normal), P(normal), P(above normal)] = [1/3, 1/3, 1/3]) for a climatological distribution [q; Eq. (5)]. Next, we examine the anomaly distribution conditioned on ENSO state against the climatological 33rd and 66th percentile thresholds, and determine the categorical probability of each tercile of the conditioned distribution (e.g., [P(below normal|Niño), P(normal |Niño), P(above normal|Niño)] = [0, 0, 1]), where the probability is determined by the number of observed categorical states ([below, normal, above]) divided by the total number. The conditioned probability distribution p [Eq. (5)] is then compared to the climatological probability distribution q using Eq. (5). This is very similar to an evaluation of the Climate Prediction Center's probabilities of tercile-based category product, and demonstrated to be an effective distance metric for ENSO effects on T2m (Schamberg et al. 2020). The KL divergence is a quantification of the information lost if a forecaster were to ignore that it was an ENSO year, and can be loosely thought of as a quantification of the forcing of the anomaly probability. Encouragingly, all of the KLPP patterns resemble the seasonal anomalies presented in (Deser et al. 2018).

Figure 13 shows the monthly T2m KLPP for DJFMA in respective El Niño (column I) and La Niña (column II) seasons, and the composite observed GPH anomaly (contour). KLPP is stippled for values significant at the 10% level. Largely, the observed KLPP matches the SN relationships displayed in Fig. 9. In agreement with the d4PDF, the results of the KLPP divergence indicate the following monthly patterns for T2m: 1) El Niño KLPP is larger than La Niña, 2) little to no KLPP exists in December for either El Niño or La Niña, 3) KLPP begins to develop over Mexico in January of El Niño and is strongest across the southern half of North America in FM, 4) January and February of La Niña years see a peak in the KLPP in the Gulf of Mexico and Florida region, 5) reliable NWNA KLPP emerges in February and peaks in March, and 6) KLPP in NWNA shifts northward in April of El Niño years and KLPP vanishes in April of La Niña years.

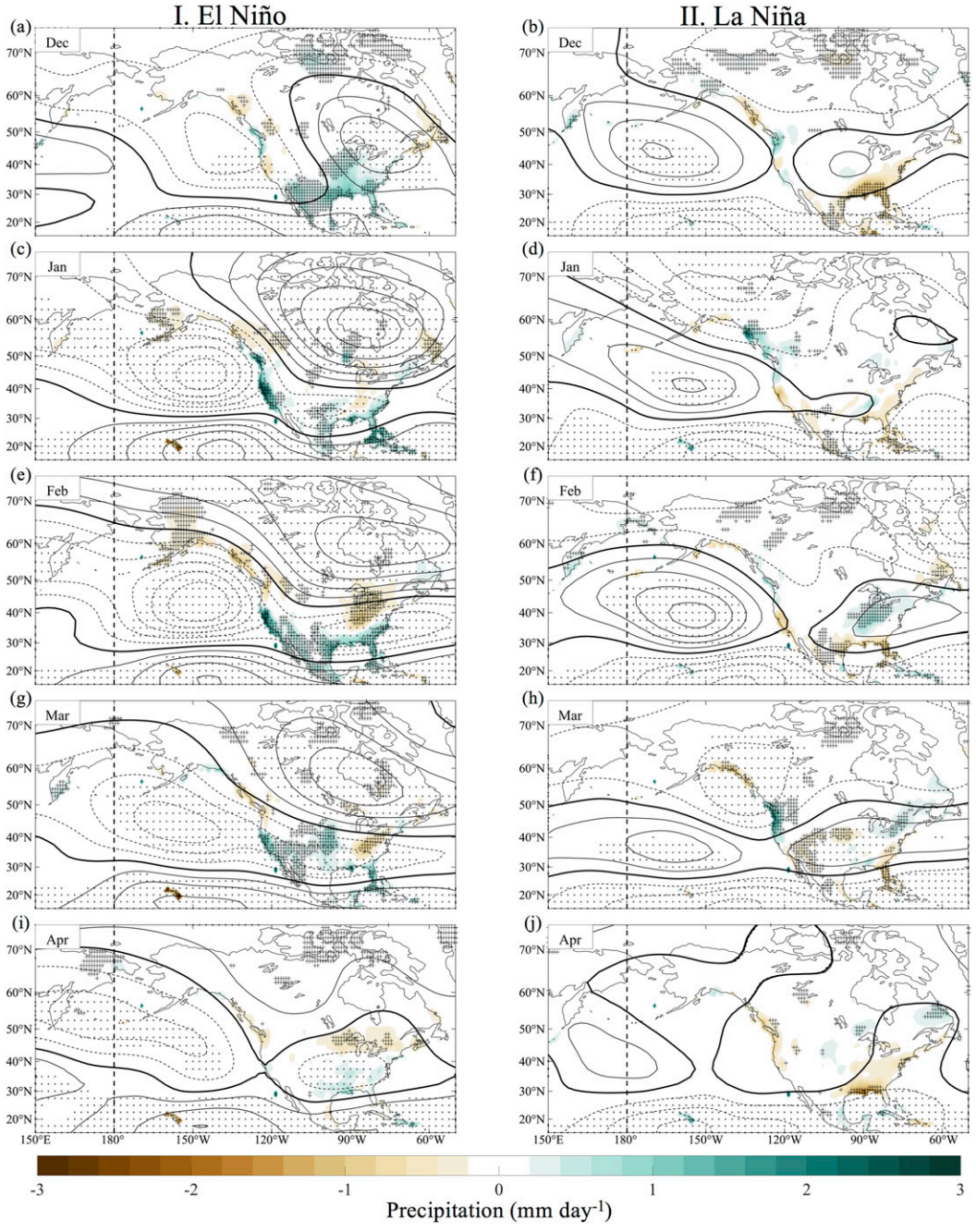

FIG. 12. (column I) El Niño and (column II) La Niña monthly composite of observed precipitation (colorfill) and 200-hPa geopotential height (contour; negative dashed). Contour intervals are set at 20 m; the 0-m contour is shown in bold. Precipitation is stippled when significant (plus sign). Geopotential height is stippled when significant (star). Significant confidence intervals are determined by bootstrap, with resampling across all years 1000 times, and examination of the 5th and 95th percentiles of the synthetic distribution.

Differences between d4PDF SN and T2M KLPP exist. We note that these could be due to the internal variability of the atmosphere and the limited number of observations or attributable to d4PDF model biases. In observations there is a clear shift of the T2m associated with the high-pressure limb of the PNA pattern in northeast Canada in January (Fig. 13c). This could be an indication of d4PDF overdispersiveness of the northern limb of the PNA pattern across the ensemble members, and a lack of ENSO forcing in the early season. This is consistent with the findings of Ayarzagüena et al. (2018) and Smith et al. (2020), which show that

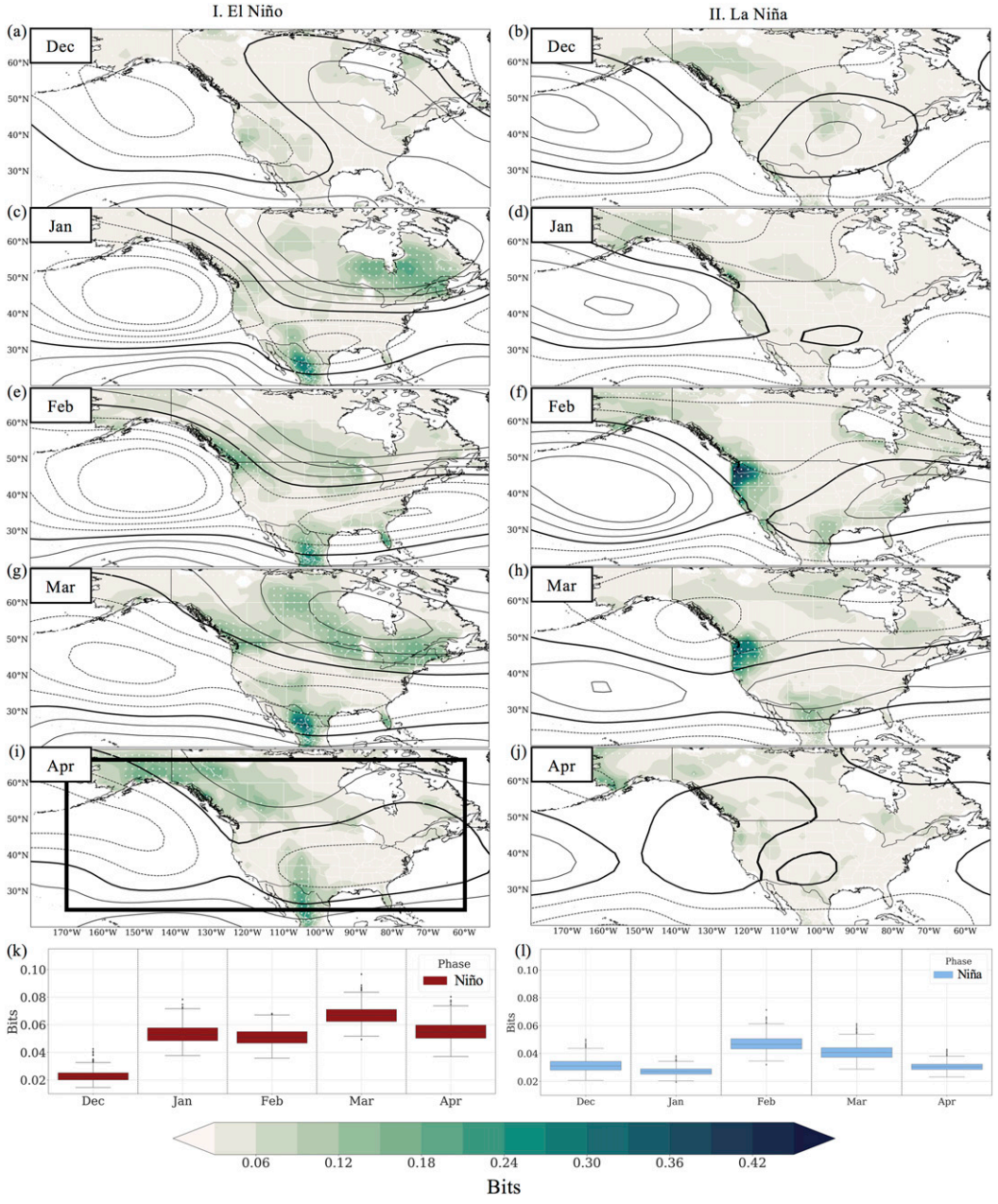

FIG. 13. (a)–(j) Observed monthly (DJFMA) T2m Kullback–Leibler divergence (KL) (tercile discrete) for (column I) El Niño and (column II) La Niña years. Significant values of KL are stippled. Significant confidence intervals are determined by bootstrap, with resampling across all years 1000 times, and examination of the 5th and 95th percentiles of the synthetic distribution. (k),(l) Land area averaged bits by month conditioned on ENSO phase (25°–65°N, 170°E–60°W, the region shown in (i)]. Contours show the observed 200-hPa GPH anomaly composite in 20-m intervals; 0-m contour shown in bold.

the NAO is more predictable than climate models typically demonstrate. Additionally, February and March of La Niña years show a distinct KL divergence spike centered over Oregon/Washington. Figures 9a and 9b show very little SN in this region. This could be attributable to an overdispersion of the Canadian limb of the PNA in La Niña seasons in the d4PDF, as a distinct trough is shown in March of observations (Fig. 12h).

The presented KLPP has implications for the contemporaneous signal between tropical ENSO SSTs and North American T2m or precipitation. However, the conditional distributions developed are dependent only on the knowledge of the contemporaneous ENSO state and the present month. The correlation between February and March Niño-3.4 indices is 0.96 and the correlation between December and March is

0.87; thus, these findings have serious implications for monthly and seasonal forecast skill.

6. Summary and discussion

Leveraging an atmosphere model ensemble, we examine the Northern Hemisphere's forced response to El Niño–Southern Oscillation (ENSO). We diagnose signal-to-noise (SN) relationships for 200-hPa geopotential height (GPH), 2-m temperature (T2m), and precipitation as a function of the amplitude and phase of tropical Pacific SST forcing, and amplitude of the natural variability at a monthly temporal resolution. Further, we verify the model findings by examining the potential predictability (PP) of those surface variables developed from observations with implications for subseasonal-to-seasonal (S2S) forecasting.

The forced teleconnection is examined with Rossby wave source (RWS) and wave activity flux analyses. The forced pattern is generally nonlinear and asymmetric with respect to categorical ENSO states, which has been noted in multiple studies (e.g., Abid et al. 2015; Johnson and Kosaka 2016; Feng et al. 2017; Zhang et al. 2019). The RWS cold season vortex stretching term is of weaker magnitude than its warm phase counterpart, resulting in nonlinear Rossby wave forcing. The forced 200-hPa GPH is a consequence of this nonlinearity with warm events showing an increased amplitude as compared to their cold phase counterpart.

Appreciable dynamic evolution occurs on monthly time scales and is potentially an important component to increasing S2S forecast skill. The forced response evolves temporally across the ENSO season (November–April), due to differences in monthly strength and location of the tropically driven upper-level divergence and the Pacific jet. The combined effect of persistent forced signal and decreased atmospheric noise results in February and March showing the greatest PP in every examined variable, and December showing weak to no PP. The dominant signal for both the internal variability and the forced response is a Pacific–North American (PNA)-like pattern (Wallace and Gutzler 1981). The pattern is particularly robust during February and March of warm phase events.

An open question remains around the forced El Niño PNA GPH anomaly in March and January. Although the RWS is nearly identical (Fig. 3), the March GPH anomaly is greater (Fig. 4). This phenomenon is observed in other AGCM SN studies (e.g., see Fig. 3 in Honda et al. 2005). Jiménez-Esteve and Domeisen (2018) show a decrease in transient eddy forcing during March, and therefore barotropic energy conversion from the jet exit region could be a potential pathway. The exact mechanism is not clear and requires focused research.

Zhou et al. (2014) notes that in a warmer climate, the large-scale 200-hPa pattern associated with El Niño shifts eastward, associated with an eastward shift of the tropical precipitation pattern. Importantly, the Pacific maximum of precipitation, coincident with the jet exit region and the PNA teleconnection pattern (~40°N, 140°W), is projected to shift eastward in a warmer climate, impacting the western coast of North America. This coincides with the peak SN region in ENSO events (Fig. 10d–g) and could lead to an increase in skill for North American West Coast precipitation prediction. Additionally, the changes in circulation lead to an eastward and southward shifted temperature anomaly due to an increase in warm advection by the Aleutian low westerlies. These patterns imprint on late-season peak SN areas (Fig. 9g) and could increase forecast skill of temperature anomalies over large swaths of North America. This necessitates an intraseasonal exploration of the changes of ENSO SN in a warmer climate.

Month-to-month ENSO dynamics and the background seasonal cycle lead to distinct teleconnection patterns. These patterns result in a myriad of signal-to-noise relationships that can be exploited for forecasting. New interest has arisen for statistical models (i.e., deep learning) for S2S forecasting owing to recent computational advances, algorithmic toolbox development, and successes in the Earth sciences (e.g., Abadi et al. 2015; Ham et al. 2019). Proper training data periods must be utilized to capture these relationships and more skill may be gleaned from intraseasonal rather than seasonal algorithm development. This study joins Ayarzagüena et al. (2018) and King et al. (2018) in warning against seasonal mean analysis due to a shifting ENSO teleconnection and noise background state.

Acknowledgments. This work is supported by the National Science Foundation under Grant AGS 1637450 and by the U.S. Army Corps of Engineers (USACE)-Cooperative Ecosystem Studies Unit (CESU), Grant W912HZ-15-2-0019 and the California Department of Water Resources Atmospheric River Program Phase 1 and 2 (Awards 4600010378 TO#15 Am 22 and 4600013361 respectively).

Data availability statement. The d4PDF dataset is available via DIAS website http://search.diasjp.net/en/dataset/d4PDF_GCM. NCEP Reanalysis derived data and PRECL precipitation data provided by the NOAA/OAR/ESRL PSL, Boulder, Colorado, USA, from their Web site at https://psl.noaa.gov/.

REFERENCES

Abadi, M., and Coauthors, 2015: TensorFlow: Large-scale machine learning on heterogeneous systems. 19 pp., https://www.tensorflow.org/about/bib. (Software available from tensorflow.org.)

Abid, M. A., I.-S. Kang, M. Almazroui, and F. Kucharski, 2015: Contribution of synoptic transients to the potential predictability of PNA circulation anomalies: El Niño versus La Niña. *J. Climate*, **28**, 8347–8362, https://doi.org/10.1175/JCLI-D-14-00497.1.

Athanasiadis, P. J., J. M. Wallace, and J. J. Wettstein, 2010: Patterns of wintertime jet stream variability and their relation to the storm tracks. *J. Atmos. Sci.*, **67**, 1361–1381, https://doi.org/10.1175/2009JAS3270.1.

Ayarzagüena, B., S. Ineson, N. J. Dunstone, M. P. Baldwin, and A. A. Scaife, 2018: Intraseasonal effects of El Niño–Southern Oscillation on North Atlantic climate. *J. Climate*, **31**, 8861–8873, https://doi.org/10.1175/JCLI-D-18-0097.1.

Barnston, A. G., and R. E. Livezey, 1987: Classification, seasonality and persistence of low-frequency atmospheric circulation patterns. *Mon. Wea. Rev.*, **115**, 1083–1126, https://doi.org/10.1175/1520-0493(1987)115⟨1083:CSAPOL⟩2.0.CO;2.

Barsugli, J. J., and P. D. Sardeshmukh, 2002: Global atmospheric sensitivity to tropical SST anomalies throughout the Indo-Pacific

basin. *J. Climate*, **15**, 3427–3442, https://doi.org/10.1175/1520-0442(2002)015⟨3427:GASTTS⟩2.0.CO;2.

Bjerknes, J., 1969: Atmospheric teleconnections from the equatorial Pacific. *Mon. Wea. Rev.*, **97**, 163–172, https://doi.org/10.1175/1520-0493(1969)097⟨0163:ATFTEP⟩2.3.CO;2.

Branstator, G., 1985: Analysis of general circulation model sea-surface temperature anomaly simulations using a linear model. Part II: Eigenanalysis. *J. Atmos. Sci.*, **42**, 2242–2254, https://doi.org/10.1175/1520-0469(1985)042⟨2242:AOGCMS⟩2.0.CO;2.

——, 1989: Low-frequency patterns induced by stationary waves. *J. Atmos. Sci.*, **47**, 629–649, https://doi.org/10.1175/1520-0469(1990)047⟨0629:LFPIBS⟩2.0.CO;2.

——, 1992: The maintenance of low-frequency atmospheric anomalies. *J. Atmos. Sci.*, **49**, 1924–1946, https://doi.org/10.1175/1520-0469(1992)049⟨1924:TMOLFA⟩2.0.CO;2.

——, and H. Teng, 2017: Tropospheric waveguide teleconnections and their seasonality. *J. Atmos. Sci.*, **74**, 1513–1532, https://doi.org/10.1175/JAS-D-16-0305.1.

Burgman, R. J., and Y. Jang, 2015: Simulated U.S. drought response to interannual and decadal Pacific SST variability. *J. Climate*, **28**, 4688–4705, https://doi.org/10.1175/JCLI-D-14-00247.1.

Chen, L.-C., H. van den Dool, E. Becker, and Q. Zhang, 2017: ENSO precipitation and temperature forecasts in the North American Multimodel Ensemble: Composite analysis and validation. *J. Climate*, **30**, 1103–1125, https://doi.org/10.1175/JCLI-D-15-0903.1.

Chen, M., and A. Kumar, 2015: Influence of ENSO SSTs on the spread of the probability density function for precipitation and land surface temperature. *Climate Dyn.*, **45**, 965–974, https://doi.org/10.1007/s00382-014-2336-9.

——, P. Xie, J. E. Janowiak, and P. A. Arkin, 2002: Global land precipitation: A 50-yr monthly analysis based on gauge observations. *J. Hydrometeor.*, **3**, 249–266, https://doi.org/10.1175/1525-7541(2002)003⟨0249:GLPAYM⟩2.0.CO;2.

Chen, W. Y., and H. M. van den Dool, 1999: Significant change of extratropical natural variability and potential predictability associated with the El Niño/Southern Oscillation. *Tellus*, **51A**, 790–802, https://doi.org/10.3402/tellusa.v51i5.14493.

Chervin, R. M., 1986: Interannual variability and seasonal climate predictability. *J. Atmos. Sci.*, **43**, 233–251, https://doi.org/10.1175/1520-0469(1986)043⟨0233:IVASCP⟩2.0.CO;2.

Chung, C. T. Y., and S. B. Power, 2015: Modelled rainfall response to strong El Niño sea surface temperature anomalies in the tropical Pacific. *J. Climate*, **28**, 3133–3151, https://doi.org/10.1175/JCLI-D-14-00610.1.

Cover, T. M., and J. A. Thomas, 2006: *Elements of Information Theory*. 2nd ed. Wiley, 748 pp.

Dai, A., 2013: The influence of the inter-decadal Pacific oscillation on us precipitation during 1923–2010. *Climate Dyn.*, **41**, 633–646, https://doi.org/10.1007/s00382-012-1446-5.

——, and T. M. L. Wigley, 2000: Global patterns of ENSO-induced precipitation. *Geophys. Res. Lett.*, **27**, 1283–1286, https://doi.org/10.1029/1999GL011140.

Davini, P., and Coauthors, 2017: Climate SPHINX: Evaluating the impact of resolution and stochastic physics parameterisations in climate simulations. *Geosci. Model Dev.*, **10**, 1383–1402, https://doi.org/10.5194/gmd-10-1383-2017.

Dawson, A., 2016: Windspharm: A high-level library for global wind field computations using spherical harmonics. *J. Open Res. Software*, **4**, e31, http://doi.org/10.5334/jors.129.

——, and T. Palmer, 2015: Simulating weather regimes: Impact of model resolution and stochastic parameterization. *Climate Dyn.*, **44**, 2177–2193, https://doi.org/10.1007/s00382-014-2238-x.

——, A. J. Matthews, and D. P. Stevens, 2010: Rossby wave dynamics of the North Pacific extra-tropical response to El Niño: Importance of the basic state in coupled GCMs. *Climate Dyn.*, **37**, 391–405, https://doi.org/10.1007/s00382-010-0854-7.

——, ——, and ——, 2011: Rossby wave dynamics of the North Pacific extra-tropical response to El Niño: Importance of the basic state in coupled GCMs. *Climate Dyn.*, **37**, 391–405, https://doi.org/10.1007/s00382-010-0854-7.

DelSole, T., 2004: Predictability and information theory. Part I: Measures of predictability. *J. Atmos. Sci.*, **61**, 2425–2440, https://doi.org/10.1175/1520-0469(2004)061<2425:PAITPI>2.0.CO;2.

Deser, C., and J. M. Wallace, 1987: El Niño events and their relation to the southern oscillation: 1925–1986. *J. Geophys. Res. Oceans*, **92**, 14 189–14 196. https://doi.org/10.1029/JC092iC13p14189.

——, and ——, 1990: Large-scale atmospheric circulation features of warm and cold episodes in the tropical Pacific. *J. Climate*, **3**, 1254–1281, https://doi.org/10.1175/1520-0442(1990)003⟨1254:LSACFO⟩2.0.CO;2.

——, I. R. Simpson, K. A. McKinnon, and A. S. Phillips, 2017: The Northern Hemisphere extratropical atmospheric circulation response to ENSO: How well do we know it and how do we evaluate models accordingly? *J. Climate*, **30**, 5059–5082, https://doi.org/10.1175/JCLI-D-16-0844.1.

——, ——, A. S. Phillips, and K. A. McKinnon, 2018: How well do we know ENSO's climate impacts over North America, and how do we evaluate models accordingly? *J. Climate*, **31**, 4991–5014, https://doi.org/10.1175/JCLI-D-17-0783.1.

Dettinger, M. D., D. R. Cayan, H. F. Diaz, and D. M. Meko, 1998: North–south precipitation patterns in western North America on interannual-to-decadal timescales. *J. Climate*, **11**, 3095–3111, https://doi.org/10.1175/1520-0442(1998)011⟨3095:NSPPIW⟩2.0.CO;2.

Feldstein, S. B., 2002: Fundamental mechanisms of the growth and decay of the PNA teleconnection pattern. *Quart. J. Roy. Meteor. Soc.*, **128**, 775–796, https://doi.org/10.1256/0035900021643683.

Feng, J., W. Chen, and Y. Li, 2017: Asymmetry of the winter extratropical teleconnections in the Northern Hemisphere associated with two types of ENSO. *Climate Dyn.*, **48**, 2135–2151, https://doi.org/10.1007/s00382-016-3196-2.

Flato, G., and Coauthors, 2013: Evaluation of climate models. *Climate Change 2013: The Physical Science Basis*, T. F. Stocker et al., Eds., Cambridge University Press, 741–866, https://doi.org/10.1017/CBO9781107415324.020.

Frauen, C., D. Dommenget, N. Tyrrell, M. Rezny, and S. Wales, 2014: Analysis of the nonlinearity of El Niño–Southern Oscillation teleconnections. *J. Climate*, **27**, 6225–6244, https://doi.org/10.1175/JCLI-D-13-00757.1.

Gadgil, S., P. V. Joseph, and N. V. Joshi, 1984: Ocean–atmosphere coupling over monsoon regions. *Nature*, **312**, 141–143, https://doi.org/10.1038/312141a0.

Gibson, P. B., D. E. Waliser, B. Guan, M. J. DeFlorio, F. M. Ralph, and D. L. Swain, 2020: Ridging associated with drought across the western and southwestern United States: Characteristics, trends, and predictability sources. *J. Climate*, **33**, 2485–2508, https://doi.org/10.1175/JCLI-D-19-0439.1.

Graham, N. E., and T. P. Barnett, 1987: Sea surface temperature, surface wind divergence, and convection over tropical oceans. *Science*, **238**, 657–659, https://doi.org/10.1126/science.238.4827.

Guo, Y., Z. Wen, R. Chen, X. Li, and X.-Q. Yang, 2019: Effect of boreal spring precipitation anomaly pattern change in the late 1990s over tropical Pacific on the atmospheric teleconnection. *Climate Dyn.*, **52**, 401–416, https://doi.org/10.1007/s00382-018-4149-8.

Hakim, G. J., 2003: Developing wave packets in the North Pacific storm track. *Mon. Wea. Rev.*, **131**, 2824–2837, https://doi.org/10.1175/1520-0493(2003)131⟨2824:DWPITN⟩2.0.CO;2.

Ham, Y.-G., J.-H. Kim, and J.-J. Luo, 2019: Deep learning for multi-year ENSO forecasts. *Nature*, **573**, 568–572, https://doi.org/10.1038/s41586-019-1559-7.

Harnik, N., R. Seager, N. Naik, M. Cane, and M. Ting, 2010: The role of linear wave refraction in the transient eddy–mean flow response to tropical Pacific SST anomalies. *Quart. J. Roy. Meteor. Soc.*, **136**, 2132–2146, https://doi.org/10.1002/qj.

Held, I. M., S. W. Lyons, and S. Nigam, 1988: Transients and the extratropical response to El Niño. *J. Atmos. Sci.*, **46**, 163–174, https://doi.org/10.1175/1520-0469(1989)046⟨0163:TATERT⟩2.0.CO;2.

Hertwig, E., J.-S. von Storch, D. Handorf, K. Dethloff, I. Fast, and T. Krismer, 2015: Effect of horizontal resolution on ECHAM6-AMIP performance. *Climate Dyn.*, **45**, 185–211, https://doi.org/10.1007/s00382-014-2396-x.

Hirahara, S., M. Ishii, and Y. Fukuda, 2014: Centennial-scale sea surface temperature analysis and its uncertainty. *J. Climate*, **27**, 57–75, https://doi.org/10.1175/JCLI-D-12-00837.1.

Hoerling, M. P., and A. Kumar, 2002: Atmospheric response patterns associated with tropical forcing. *J. Climate*, **15**, 2184–2203, https://doi.org/10.1175/1520-0442(2002)015⟨2184:ARPAWT⟩2.0.CO;2.

——, ——, and M. Zhong, 1997: El Niño, La Niña, and the nonlinearity of their teleconnections. *J. Climate*, **10**, 1769–1786, https://doi.org/10.1175/1520-0442(1997)010⟨1769:ENOLNA⟩2.0.CO;2.

——, ——, and T. Xu, 2001: Robustness of the nonlinear climate response to ENSO's extreme phases. *J. Climate*, **14**, 1277–1293, https://doi.org/10.1175/1520-0442(2001)014⟨1277:ROTNCR⟩2.0.CO;2.

Honda, M., and H. Nakamura, 2001: Interannual seesaw between the Aleutian and Icelandic lows. Part II: Its significance in the interannual variability over the wintertime Northern Hemisphere. *J. Climate*, **14**, 4512–4529, https://doi.org/10.1175/1520-0442(2001)014<4512:ISBTAA>2.0.CO;2.

——, ——, J. Ukita, I. Kousaka, and K. Takeuchi, 2001: Interannual seesaw between the Aleutian and Icelandic lows. Part I: Seasonal dependence and life cycle. *J. Climate*, **14**, 1029–1042, https://doi.org/10.1175/1520-0442(2001)014⟨1029:ISBTAA⟩2.0.CO;2.

——, Y. Kushnir, H. Nakamura, S. Yamane, and S. E. Zebiak, 2005: Formation, mechanisms, and predictability of the Aleutian–Icelandic low seesaw in ensemble AGCM simulations. *J. Climate*, **18**, 1423–1434, https://doi.org/10.1175/JCLI3353.1.

Huang, J., K. Higuchi, and A. Shabbar, 1998: The relationship between the North Atlantic Oscillation and El Niño–Southern Oscillation. *Geophys. Res. Lett.*, **25**, 2707–2710, https://doi.org/10.1029/98GL01936.

Jiménez-Esteve, B., and D. I. V. Domeisen, 2018: The tropospheric pathway of the ENSO–North Atlantic teleconnection. *J. Climate*, **31**, 4563–4584, https://doi.org/10.1175/JCLI-D-17-0716.1.

——, and ——, 2019: Nonlinearity in the North Pacific atmospheric response to a linear ENSO forcing. *Geophys. Res. Lett.*, **46**, 2271–2281, https://doi.org/10.1029/2018GL081226.

Johnson, N. C., 2013: How many ENSO flavors can we distinguish? *J. Climate*, **26**, 4816–4827, https://doi.org/10.1175/JCLI-D-12-00649.1.

——, and S.-P. Xie, 2010: Changes in the sea surface temperature threshold for tropical convection. *Nat. Geosci.*, **3**, 842–845, https://doi.org/10.1038/ngeo1008.

——, and Y. Kosaka, 2016: The impact of eastern equatorial Pacific convection on the diversity of boreal winter El Niño teleconnection patterns. *Climate Dyn.*, **47**, 3737–3765, https://doi.org/10.1007/s00382-016-3039-1.

——, D. C. Collins, S. B. Feldstein, M. L. L'Heureux, and E. E. Riddle, 2014: Skillful wintertime North American temperature forecasts out to 4 weeks based on the state of ENSO and the MJO. *Wea. Forecasting*, **29**, 23–38, https://doi.org/10.1175/WAF-D-13-00102.1.

Jong, B.-T., M. Ting, and R. Seager, 2016: El Niño's impact on California precipitation: Seasonality, regionality, and El Niño intensity. *Environ. Res. Lett.*, **11**, 054021, https://doi.org/10.1088/1748-9326/11/5/054021.

Kalnay, E., and Coauthors, 1996: The NCEP/NCAR 40-Year Reanalysis Project. *Bull. Amer. Meteor. Soc.*, **77**, 437–472, https://doi.org/10.1175/1520-0477(1996)077⟨0437:TNYRP⟩2.0.CO;2.

Kamae, Y., and Coauthors, 2017: Forced response and internal variability of summer climate over western North America. *Climate Dyn.*, **49**, 403–417, https://doi.org/10.1007/s00382-016-3350-x.

Kang, I.-S., and J. Shukla, 2006: Dynamic seasonal prediction and predictability of the monsoon. *The Asian Monsoon*, B. Wang, Ed., Springer, 585–612, https://doi.org/10.1007/3-540-37722-0_15.

——, J.-S. Kug, M.-J. Lim, and D.-H. Choi, 2011: Impact of transient eddies on extratropical seasonal-mean predictability in DEMETER models. *Climate Dyn.*, **V**, 509–519, https://doi.org/10.1007/s00382-010-0873-4.

King, M. P., I. Herceg-Bulić, I. Bladé, J. García-Serrano, N. Keenlyside, F. Kucharski, C. Li, and S. Sobolowski, 2018: Importance of late fall ENSO teleconnection in the Euro-Atlantic sector. *Bull. Amer. Meteor. Soc.*, **99**, 1337–1343, https://doi.org/10.1175/BAMS-D-17-0020.1.

Kleeman, R., 2002: Measuring dynamical prediction utility using relative entropy. *J. Atmos. Sci.*, **59**, 2057–2072, https://doi.org/10.1175/1520-0469(2002)059⟨2057:MDPUUR⟩2.0.CO;2.

Kullback, S., 1997: *Information Theory and Statistics*. 2nd ed. Dover, 399 pp.

Kumar, A., and M. P. Hoerling, 1995: Prospects and limitations of seasonal atmospheric GCM predictions. *Bull. Amer. Meteor. Soc.*, **76**, 335–345, https://doi.org/10.1175/1520-0477(1995)076⟨0335:PALOSA⟩2.0.CO;2.

——, and ——, 1998: Annual cycle of Pacific–North American seasonal predictability associated with different phases of ENSO. *J. Climate*, **11**, 3295–3308, https://doi.org/10.1175/1520-0442(1998)011⟨3295:ACOPNA⟩2.0.CO;2.

——, A. G. Barnston, P. Peng, M. P. Hoerling, and L. Goddard, 2000: Changes in the spread of the variability of the seasonal mean atmospheric states associated with ENSO. *J. Climate*, **13**, 3139–3151, https://doi.org/10.1175/1520-0442(2000)013⟨3139:CITSOT⟩2.0.CO;2.

——, Q. Zhang, P. Peng, and B. Jha, 2005: SST-forced atmospheric variability in an atmospheric general circulation model. *J. Climate*, **18**, 3953–3967, https://doi.org/10.1175/JCLI3483.1.

Lau, N.-C., and M. J. Nath, 1996: The role of the "atmospheric bridge" in linking tropical Pacific ENSO events to extratropical SST anomalies. *J. Climate*, **9**, 2036–2057, https://doi.org/10.1175/1520-0442(1996)009⟨2036:TROTBI⟩2.0.CO;2.

Li, Y., and N.-C. Lau, 2012: Impact of ENSO on the atmospheric variability over the North Atlantic in late winter—Role of transient eddies. *J. Climate*, **25**, 320–342, https://doi.org/10.1175/JCLI-D-11-00037.1.

MacKay, D. J., 2003: *Information Theory, Inference and Learning Algorithms*. Cambridge University Press, 628 pp.

Matsumura, S., G. Huang, S.-P. Xie, and K. Yamazaki, 2010: SST-forced and internal variability of the atmosphere in an ensemble GCM simulation. *J. Meteor. Soc. Japan*, **88**, 43–62, https://doi.org/10.2151/jmsj.2010-104.

Meehl, G. A., and A. Hu, 2006: Megadroughts in the Indian monsoon region and southwest North America and a mechanism for associated multidecadal Pacific sea surface temperature anomalies. *J. Climate*, **19**, 1605–1623, https://doi.org/10.1175/JCLI3675.1.

Mei, W., Y. Kamae, S.-P. Xie, and K. Yoshida, 2019: Variability and predictability of North Atlantic hurricane frequency in a large ensemble of high-resolution atmospheric simulations. *J. Climate*, **32**, 3153–3167, https://doi.org/10.1175/JCLI-D-18-0554.1.

Mizuta, R., and Coauthors, 2012: Climate simulations using MRI-AGCM3.2 with 20-km grid. *J. Meteor. Soc. Japan*, **90A**, 233–258, https://doi.org/10.2151/jmsj.2012-A12.

——, and Coauthors, 2017: Over 5,000 years of ensemble future climate simulations by 60-km global and 20-km regional atmospheric models. *Bull. Amer. Meteor. Soc.*, **98**, 1383–1398, https://doi.org/10.1175/BAMS-D-16-0099.1.

Mo, K. C., and R. E. Livezey, 1986: Tropical-extratropical geopotential height teleconnections during the Northern Hemisphere winter. *Mon. Wea. Rev.*, **114**, 2488–2515, https://doi.org/10.1175/1520-0493(1986)114⟨2488:TEGHTD⟩2.0.CO;2.

Murakami, H., R. Mizuta, and E. Shindo, 2012: Future changes in tropical cyclone activity projected by multi-physics and multi-SST ensemble experiments using the 60-km-mesh MRI-AGCM. *Climate Dyn.*, **39**, 2569–2584, https://doi.org/10.1007/s00382-011-1223-x.

Naoi, M., Y. Kamae, H. Ueda, and W. Mei, 2020: Impacts of seasonal transitions of ENSO on atmospheric river activity over East Asia. *J. Meteor. Soc. Japan*, **98**, 655–668, https://doi.org/10.2151/jmsj.2020-027.

Neelin, J. D., F.-F. Jin, and H.-H. Syu, 2000: Variations in ENSO phase locking. *J. Climate*, **13**, 2570–2590, https://doi.org/10.1175/1520-0442(2000)013⟨2570:VIEPL⟩2.0.CO;2.

Newman, M., and P. D. Sardeshmukh, 1998: The impact of the annual cycle on the North Pacific/North American response to remote low-frequency forcing. *J. Atmos. Sci.*, **55**, 1336–1353, https://doi.org/10.1175/1520-0469(1998)055⟨1336:TIOTAC⟩2.0.CO;2.

——, S.-I. Shin, and M. A. Alexander, 2011: Natural variation in ENSO flavors. *Geophys. Res. Lett.*, **38**, L14705, https://doi.org/10.1029/2011GL047658.

Nie, Y., Y. Zhang, X.-Q. Yang, and H.-L. Ren, 2019: Winter and summer Rossby wave sources in the CMIP5 models. *Earth Space Sci.*, **6**, 1831–1846, https://doi.org/10.1029/2019EA000674.

Norris, J. R., 2000: Interannual and interdecadal variability in the storm track, cloudiness, and sea surface temperature over the summertime North Pacific. *J. Climate*, **13**, 422–430, https://doi.org/10.1175/1520-0442(2000)013⟨0422:IAIVIT⟩2.0.CO;2.

Orsolini, Y. J., N. G. Kvamstø; I. T. Kindem, M. Honda, and H. Nakamura, 2008: Influence of the Aleutian-Icelandic low seesaw and ENSO onto the stratosphere in ensemble winter hindcasts. *J. Meteor. Soc. Japan*, **86**, 817–825, https://doi.org/10.2151/jmsj.86.817.

Peng, P., and A. Kumar, 2005: A large ensemble analysis of the influence of tropical SSTs on seasonal atmospheric variability. *J. Climate*, **18**, 1068–1085, https://doi.org/10.1175/JCLI-3314.1.

Philander, S. G., 1989: *El Niño, La Niña, and the Southern Oscillation*. International Geophysics Series, Vol. 46, Elsevier, 289 pp.

Pinto, J. G., M. Reyers, and U. Ulbrich, 2011: The variable link between PNA and NAO in observations and in multi-century CGCM simulations. *Climate Dyn.*, **36**, 337–354, https://doi.org/10.1007/s00382-010-0770-x.

Ropelewski, C. F., and M. S. Halpert, 1986: North American precipitation and temperature patterns associated with the El Niño/Southern Oscillation (ENSO). *Mon. Wea. Rev.*, **114**, 2352–2362, https://doi.org/10.1175/1520-0493(1986)114⟨2352:NAPATP⟩2.0.CO;2.

Roulston, M. S., and L. A. Smith, 2002: Evaluating probabilistic forecasts using information theory. *Mon. Wea. Rev.*, **130**, 1653–1660, https://doi.org/10.1175/1520-0493(2002)130⟨1653:EPFUIT⟩2.0.CO;2.

Rowell, D. P., 1998: Assessing potential seasonal predictability with an ensemble of multidecadal GCM simulations. *J. Climate*, **11**, 109–120, https://doi.org/10.1175/1520-0442(1998)011⟨0109:APSPWA⟩2.0.CO;2.

Sardeshmukh, P. D., and B. J. Hoskins, 1988: The generation of global rotational flow by steady idealized tropical divergence. *J. Atmos. Sci.*, **45**, 1228–1251, https://doi.org/10.1175/1520-0469(1988)045⟨1228:TGOGRF⟩2.0.CO;2.

——, G. P. Compo, and C. Penland, 2000: Changes of probability associated with El Niño. *J. Climate*, **13**, 4268–4286, https://doi.org/10.1175/1520-0442(2000)013⟨4268:COPAWE⟩2.0.CO;2.

Scaife, A. A., and D. Smith, 2018: A signal-to-noise paradox in climate science. *npj Climate Atmos. Sci.*, **1**, 28, https://doi.org/10.1038/s41612-018-0038-4.

Schamberg, G., W. Chapman, S.-P. Xie, and T. P. Coleman, 2020: Direct and indirect effects—An information theoretic perspective. *Entropy*, **22**, 854, https://doi.org/10.3390/e22080854.

Schubert, S. D., M. J. Suarez, Y. Chang, and G. Branstator, 2001: The impact of ENSO on extratropical low-frequency noise in seasonal forecasts. *J. Climate*, **14**, 2351–2365, https://doi.org/10.1175/1520-0442(2001)014⟨2351:TIOEOE⟩2.0.CO;2.

Seager, R., Y. Kushnir, C. Herweijer, N. Naik, and J. Velez, 2005: Modeling of tropical forcing of persistent droughts and pluvials over western North America: 1856–2000. *J. Climate*, **18**, 4065–4088, https://doi.org/10.1175/JCLI3522.1.

——, N. Naik, M. Ting, M. A. Cane, N. Harnik, and Y. Kushnir, 2010: Adjustment of the atmospheric circulation to tropical Pacific SST anomalies: Variability of transient eddy propagation in the Pacific–North America sector. *Quart. J. Roy. Meteor. Soc.*, **136**, 277–296, https://doi.org/10.1002/qj.588.

Shi, W., N. Schaller, D. MacLeod, T. N. Palmer, and A. Weisheimer, 2015: Impact of hindcast length on estimates of seasonal climate predictability. *Geophys. Res. Lett.*, **42**, 1554–1559, https://doi.org/10.1002/2014GL062829.

Shukla, J., and J. M. Wallace, 1983: Numerical simulation of the atmospheric response to equatorial Pacific sea surface temperature anomalies. *J. Atmos. Sci.*, **40**, 1613–1630, https://doi.org/10.1175/1520-0469(1983)040⟨1613:NSOTAR⟩2.0.CO;2.

Siegert, S., D. B. Stephenson, P. G. Sansom, A. A. Scaife, R. Eade, and A. Arribas, 2016: A Bayesian framework for verification and recalibration of ensemble forecasts: How uncertain is NAO predictability? *J. Climate*, **29**, 995–1012, https://doi.org/10.1175/JCLI-D-15-0196.1.

Simmons, A. J., J. M. Wallace, and G. W. Branstator, 1983: Barotropic wave propagation and instability, and atmospheric teleconnection patterns. *J. Atmos. Sci.*, **40**, 1363–1392, https://doi.org/10.1175/1520-0469(1983)040⟨1363:BWPAIA⟩2.0.CO;2.

Smith, D. M., and Coauthors, 2020: North Atlantic climate far more predictable than models imply. *Nature*, **583**, 796–800, https://doi.org/10.1038/s41586-020-2525-0.

Souders, M. B., B. A. Colle, and E. K. M. Chang, 2014: The climatology and characteristics of Rossby wave packets using a feature-based tracking technique. *Mon. Wea. Rev.*, **142**, 3528–3548, https://doi.org/10.1175/MWR-D-13-00371.1.

Stephenson, D. B., V. Pavan, and R. Bojariu, 2000: Is the North Atlantic Oscillation a random walk? *Int. J. Climatol.*, **20**, 1–18, https://doi.org/10.1002/(SICI)1097-0088(200001)20:1<1::AID-JOC456>3.0.CO;2-P.

Straus, D. M., and J. Shukla, 1997: Variations of midlatitude transient dynamics associated with ENSO. *J. Atmos. Sci.*, **54**, 777–790, https://doi.org/10.1175/1520-0469(1997)054⟨0777:VOMTDA⟩2.0.CO;2.

Takaya, K., and H. Nakamura, 2001: A formulation of a phase-independent wave-activity flux for stationary and migratory quasigeostrophic eddies on a zonally varying basic flow. *J. Atmos. Sci.*, **58**, 608–627, https://doi.org/10.1175/1520-0469(2001)058⟨0608:AFOAPI⟩2.0.CO;2.

Trascasa-Castro, P., A. C. Maycock, Y. Y. Scott Yiu, and J. K. Fletcher, 2019: On the linearity of the stratospheric and Euro-Atlantic sector response to ENSO. *J. Climate*, **32**, 6607–6626, https://doi.org/10.1175/JCLI-D-18-0746.1.

Trenberth, K. E., G. W. Branstator, D. Karoly, A. Kumar, N.-C. Lau, and C. Ropelewski, 1998: Progress during TOGA in understanding and modeling global teleconnections associated with tropical sea surface temperatures. *J. Geophys. Res. Oceans*, **103**, 14 291–14 324. https://doi.org/10.1029/97JC01444.

Wallace, J. M., and D. S. Gutzler, 1981: Teleconnections in the geopotential height field during the Northern Hemisphere winter. *Mon. Wea. Rev.*, **109**, 784–812, https://doi.org/10.1175/1520-0493(1981)109⟨0784:TITGHF⟩2.0.CO;2.

Weisheimer, A., D. Decremer, D. MacLeod, C. O'Reilly, T. N. Stockdale, S. Johnson, and T. N. Palmer, 2019: How confident are predictability estimates of the winter North Atlantic Oscillation? *Quart. J. Roy. Meteor. Soc.*, **145**, 140–159, https://doi.org/10.1002/qj.3446.

Xie, S.-P., Q. Peng, Y. Kamae, X.-T. Zheng, H. Tokinaga, and D. Wang, 2018: Eastern Pacific ITCZ dipole and ENSO diversity. *J. Climate*, **31**, 4449–4462, https://doi.org/10.1175/JCLI-D-17-0905.1.

Yang, X.-Q., J. L. Anderson, and W. F. Stern, 1998: Reproducible forced modes in AGCM ensemble integrations and potential predictability of atmospheric seasonal variations in the extratropics. *J. Climate*, **11**, 2942–2959, https://doi.org/10.1175/1520-0442(1998)011⟨2942:RFMIAE⟩2.0.CO;2.

Zhang, T., M. P. Hoerling, J. Perlwitz, D.-Z. Sun, and D. Murray, 2011: Physics of U.S. surface temperature response to ENSO. *J. Climate*, **24**, 4874–4887, https://doi.org/10.1175/2011JCLI3944.1.

——, J. Perlwitz, and M. P. Hoerling, 2014: What is responsible for the strong observed asymmetry in teleconnections between El Niño and La Niña? *Geophys. Res. Lett.*, **41**, 1019–1025, https://doi.org/10.1002/2013GL058964.

——, M. P. Hoerling, J. Perlwitz, and T. Xu, 2016: Forced atmospheric teleconnections during 1979–2014. *J. Climate*, **29**, 2333–2357, https://doi.org/10.1175/JCLI-D-15-0226.1.

Zhang, W., and B. Kirtman, 2019: Estimates of decadal climate predictability from an interactive ensemble model. *Geophys. Res. Lett.*, **46**, 3387–3397, https://doi.org/10.1029/2018GL081307.

——, Z. Wang, M. F. Stuecker, A. G. Turner, F.-F. Jin, and X. Geng, 2019: Impact of ENSO longitudinal position on teleconnections to the NAO. *Climate Dyn.*, **52**, 257–274, https://doi.org/10.1007/s00382-018-4135-1.

Zheng, X., M. Sugi, and C. S. Frederiksen, 2004: Interannual variability and predictability in an ensemble of climate simulations with the MRI-JMA AGCM. *J. Meteor. Soc. Japan*, **82**, 1–18, https://doi.org/10.2151/jmsj.82.1.

Zhou, Z.-Q., S.-P. Xie, X.-T. Zheng, Q. Liu, and H. Wang, 2014: Global warming–induced changes in El Niño teleconnections over the North Pacific and North America. *J. Climate*, **27**, 9050–9064, https://doi.org/10.1175/JCLI-D-14-00254.1.